

LECTURE 8: Basic Methods in Antenna Measurements

(Antenna ranges and anechoic chambers. Measuring far-field patterns, gain, directivity, radiation efficiency, input impedance and polarization.)

1. Introduction*

Many of the basic methods for measuring antenna characteristics were developed before and during World War II. However, new approaches and measurement technologies continue to emerge boosted by the rapid growth of mobile communications and wireless networks. The methods for measuring antenna far-field patterns, polarization, input impedance, gain and directivity have been developed in conjunction with the design of novel radiating structures, which are needed in the telecommunications and radar technologies.

Antenna metrology requires not only sound theoretical background in antenna theory and radiation but also sophisticated equipment capable of providing the necessary accuracy and purity of the measured data. Commercial equipment specifically designed for antenna measurements became available in the 1960s due, in part, to the requirements of the aerospace, space and defence industries.

The antenna measurement equipment includes: antenna ranges, antenna positioners, pattern recorders, scalar and/or vector network analyzers, signal generators, antenna gain standards, etc. Later on, sophisticated computer systems were developed to provide automated control of pattern measurements as well as fast calculations related to antenna directivity, 2-D to 3-D pattern conversion, near-to-far field transformations (in compact antenna ranges), etc.

2. General Requirements for Antenna Measurement Procedures*

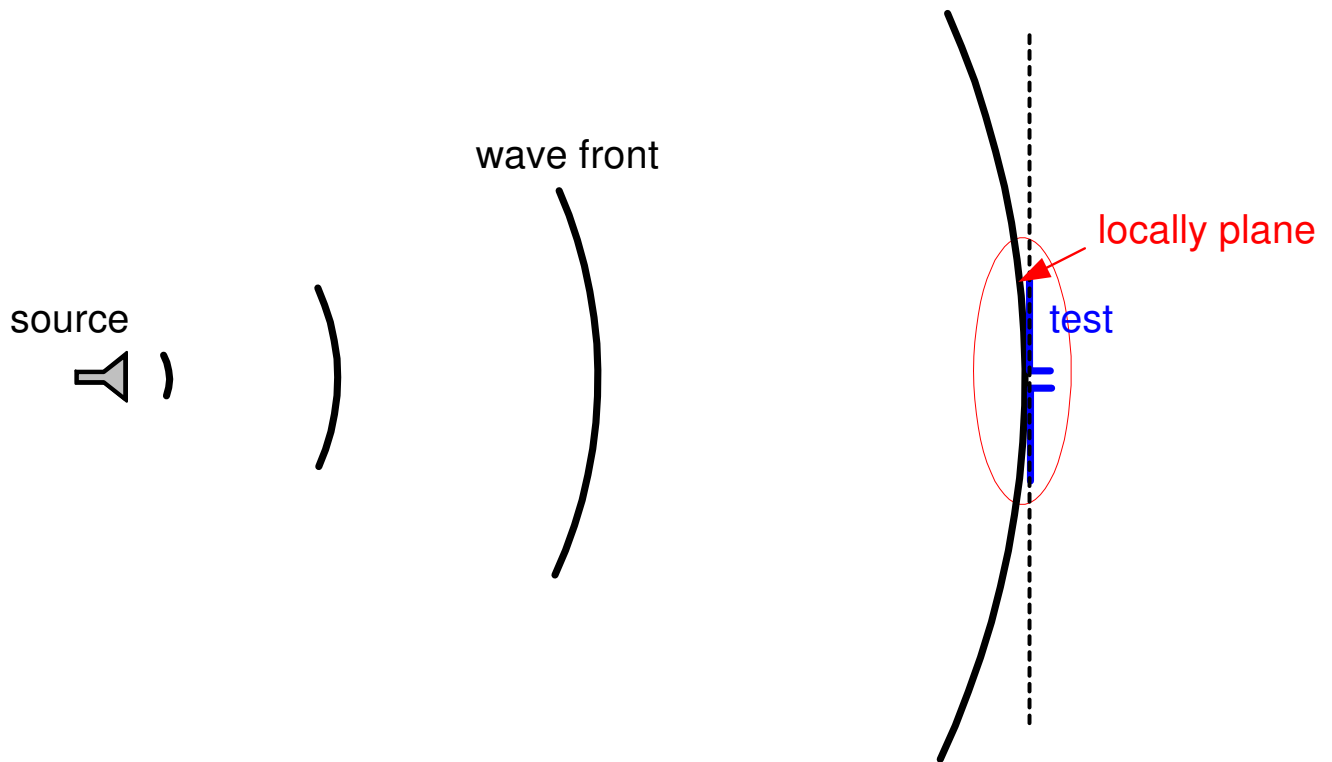
The ideal condition for measuring the far-field pattern and antenna gain is an *illumination by a uniform plane wave*. This is a wave, which has a plane wave front with the field vectors being constant over an area that extends well beyond the aperture of the antenna under test (AUT). For example, the **E** field vector of a uniform non-attenuating plane wave propagating in the $+z$ -direction is described by the 1-D wave expression

$$\mathbf{E}(z) = \hat{\mathbf{p}}_w E_m e^{-jkz}. \quad (1)$$

Here, $\hat{\mathbf{p}}_w$ is the wave polarization vector, which must remain constant within

the volume of the AUT. The same holds for the magnitude E_m , which must remain constant across the AUT aperture.

In practice, antennas generate far fields in 3-D space which are closely approximated by spherical wave fronts when the observation point is sufficiently far from the source. Also, at large distances from the source antenna, the curvature of the phase front is small at the aperture of the AUT and it is well approximated by a uniform plane wave.

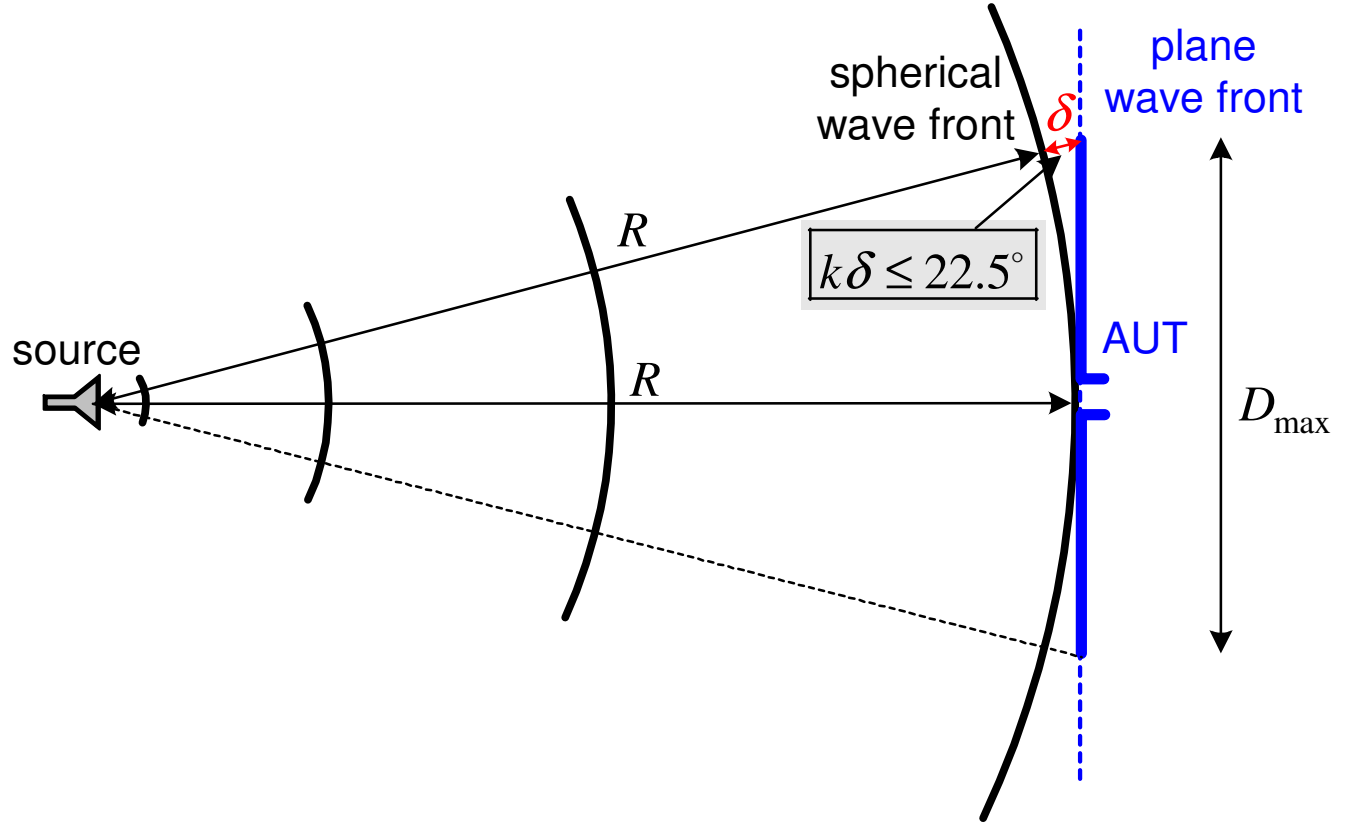


If the distance from the source is equal or greater than the inner boundary of the far-field region $R_{\min} = 2D_{\max,Tx}^2 / \lambda$, then the maximum phase difference between the actual incident field and its far-zone approximation (remember the 1st order binomial approximation $R \approx r - D_{\max,Tx} / 2$) does not exceed $\epsilon_{\max} \approx 22.5^\circ = \pi / 8$ rad. Here, $D_{\max,Tx}$ is the maximum dimension of the source (or transmitting) antenna.

Conversely, we can show that if $D_{\max,Rx} \equiv D_{\max}$ is the maximum dimension of the receiving AUT, a distance

$$R_{\min} = 2D_{\max}^2 / \lambda \quad (2)$$

from the source of a spherical wave ensures that the maximum phase difference between a plane wave and the spherical wave at the aperture of the AUT is $\epsilon_{\max} \approx 22.5^\circ = \pi/8$ rad. Consider a source of a spherical wave and an AUT located a distance R away.



The largest phase difference between the spherical wave and the plane wave appears at the edges of the AUT, which corresponds to the difference in the wave paths δ . This phase difference must fulfil the requirement:

$$k\delta \leq \pi/8. \quad (3)$$

The difference in the wave paths δ is determined by noticing that

$$(R + \delta)^2 = R^2 + (D_{\max}/2)^2. \quad (4)$$

The real-positive solution of this quadratic equation for δ is

$$\delta = \sqrt{R^2 + (D_{\max}/2)^2} - R. \quad (5)$$

Next, the above expression is approximated by the use of the binomial

expansion (the first two terms only) as

$$\delta = R \left[\sqrt{1 + \left(\frac{D_{\max}}{2R} \right)^2} - 1 \right] \approx R \left[1 + \frac{1}{2} \left(\frac{D_{\max}}{2R} \right)^2 - 1 \right] = \frac{D_{\max}^2}{8R}. \quad (6)$$

The minimum distance from the source of the spherical wave is now determined from the requirement in (3),

$$k \frac{D_{\max}^2}{8R} = \frac{2\pi}{\lambda} \frac{D_{\max}^2}{8R} \leq \frac{\pi}{8}. \quad (7)$$

Thus,

$$R_{\min} = 2D_{\max}^2 / \lambda. \quad (8)$$

It is now clear that the antenna far-field characteristics must be measured at a sufficiently large distance between the source antenna and the AUT. ***This distance must be greater than the larger of the two inner limits of the far zones of the transmitting and receiving antennas, i.e., the two antennas must be in each other's far zones.***

The above requirement leads to a major difficulty in antenna measurements – large separation distances are required between the source antenna and the AUT. The larger the AUT, the larger the measurement site. While the size of the site may not be a problem, securing its reflection-free, noise-free, and EM interference-free environment is extremely difficult.

Special attention must be paid to minimizing unwanted reflections from nearby objects (equipment, personnel, buildings), from the ground or the walls of the site. This makes the open sites for antenna measurements (***open ranges***) a rare commodity since they have to provide free-space propagation. Such ideal conditions are found only in unpopulated (desert) areas of predominantly flat terrain. The other alternative is offered by indoor chambers (***anechoic chambers***), which minimize reflections by special wall lining with RF/microwave absorbing material. They are much preferred to open ranges because of their controlled environment. Unfortunately, the anechoic chambers are very expensive and often they cannot accommodate large antennas.

There are cases in which the antenna operates in a very specific environment (mounted on an aircraft, mobile system, etc.). Then, it is better to measure the antenna as it is mounted, i.e., in its own environment. Such measurements are

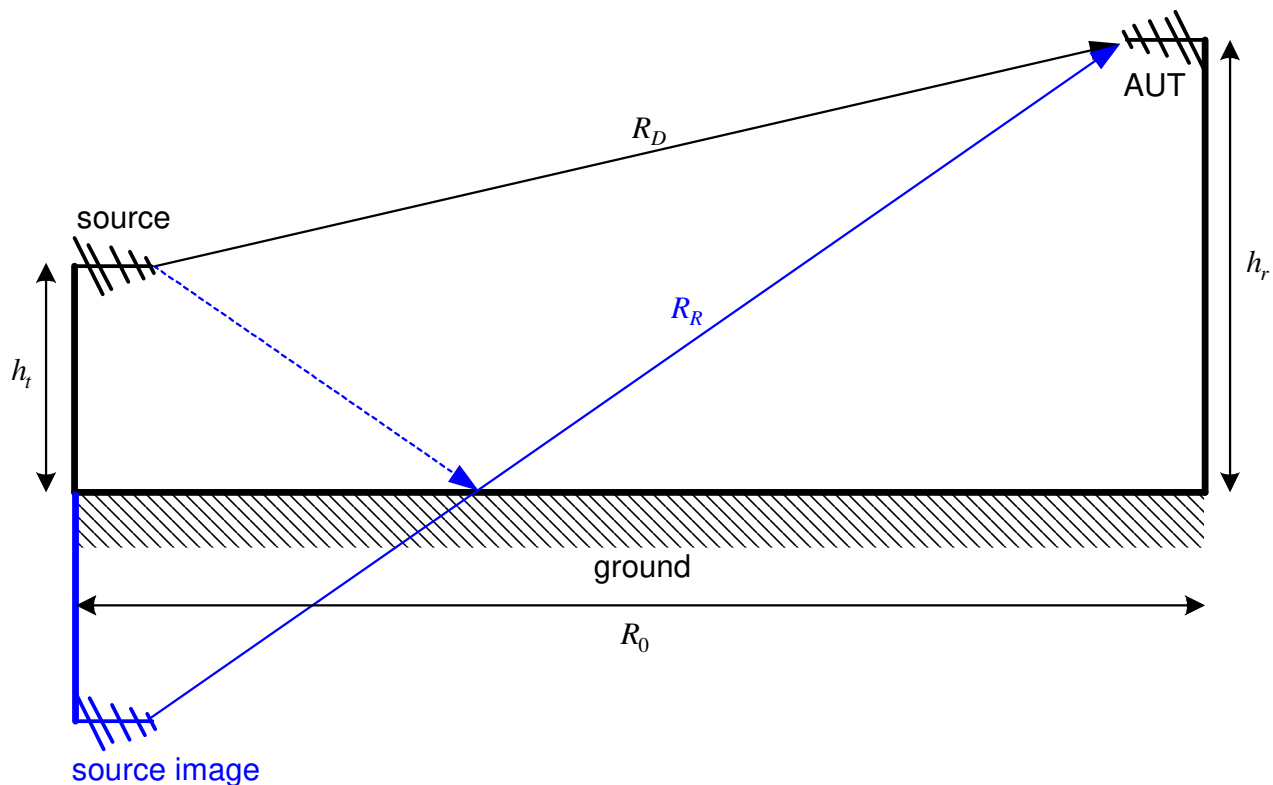
very specific and usually cannot be performed in anechoic chambers.

Below is a summary of the challenges in antenna measurements:

- affected by unwanted reflections;
- often require too large separation distances;
- very complicated when a whole antenna system (e.g., on-craft mounted antenna) is to be measured;
- outdoor sites have uncontrollable EM environment, which, besides all, depends on the weather;
- indoor sites cannot accommodate large antenna systems;
- the instrumentation is expensive.

3. Antenna Ranges (AR)*

The antenna measurement sites are called *antenna ranges* (AR). They can be categorized as outdoor ranges and indoor ranges (anechoic chambers). According to the principle of measurement, they can be also categorized as reflection ranges, free-space ranges, and compact ranges.



The reflection ranges are designed so that the direct and reflected (usually from ground) waves interfere constructively and form a uniform (in both magnitude and phase) wave front in the region of the AUT. Such a region is called the ***quite zone***. Reflection ranges are usually of the outdoor type. They are used to measure antennas of moderately broad patterns operating in the UHF frequency bands (500 MHz to 1000 MHz).

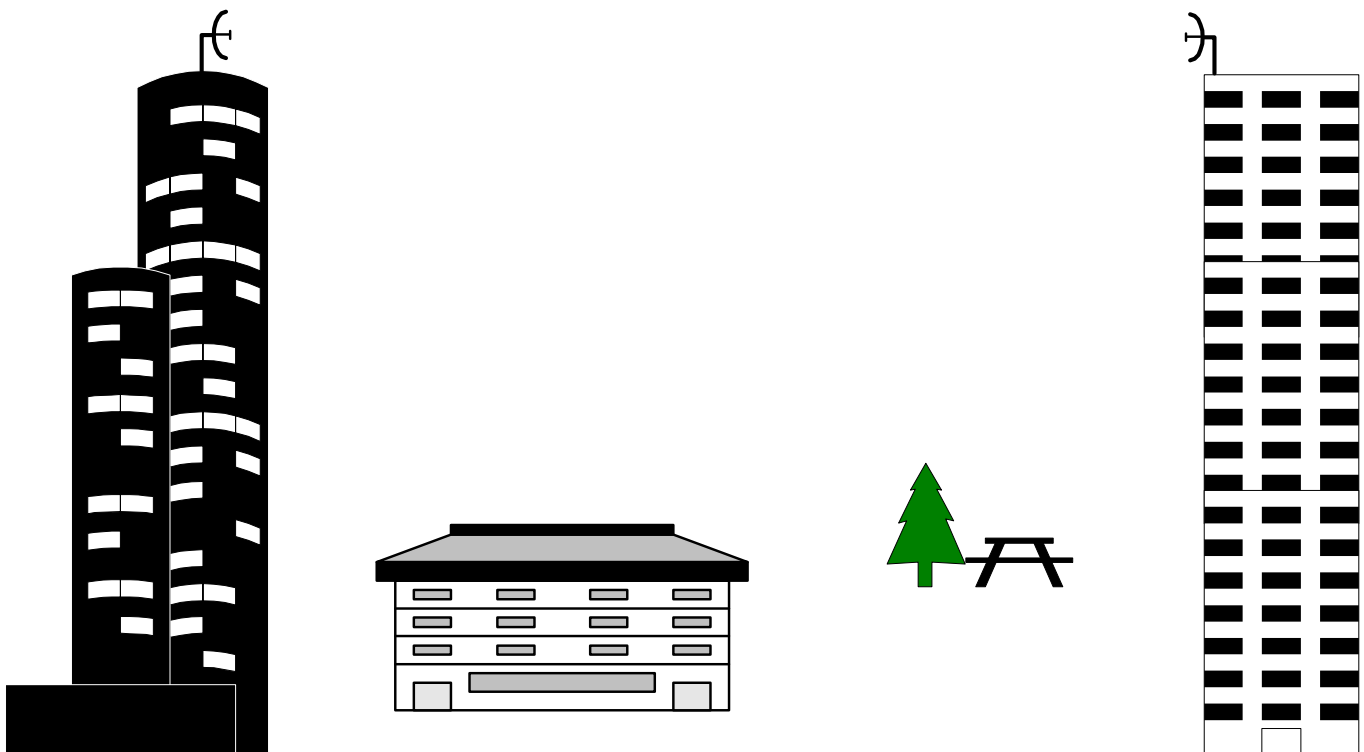
The reflection-range design is complicated and depends on the reflection coefficient of the ground (the range surface), its smoothness, as well as the pattern of the source antenna. The parameter to be determined is the height h_r of the mast, on which the AUT is to be mounted, provided that the height of the transmitting antenna h_t is known. More information can be found in

L.H. Hemming and R.A. Heaton, “Antenna gain calibration on a ground reflection range,” *IEEE Trans. on Antennas and Propagation*, vol. AP-21, pp. 532-537, July 1977.

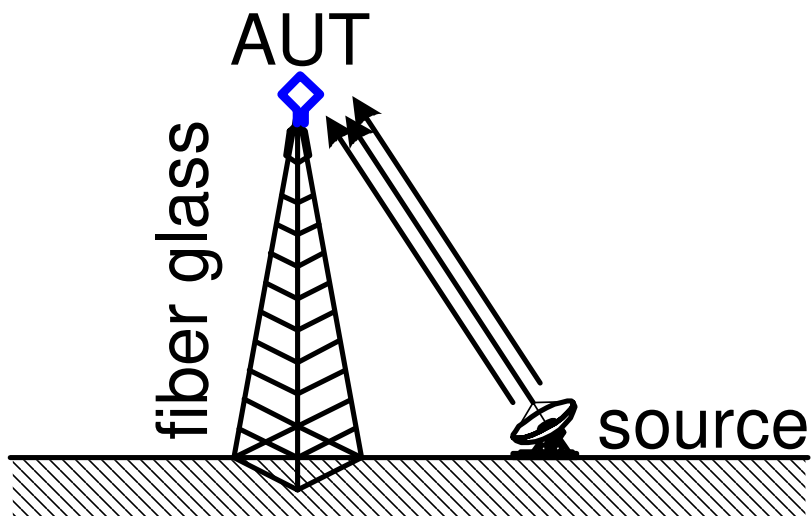
The free-space ranges provide reflection-free propagation. They can be outdoor or indoor. ***Outdoor free-space ranges*** are carefully built in such a way that reflections from buildings and other objects are minimized. They can be realized as *elevated ranges* and *slant ranges*. ***Indoor ranges*** (anechoic chambers) suppress reflections (echoes) by lining the walls, the floor and the ceiling with special RF/microwave absorbers.

The elevated ranges are characterized by the following features:

- Both antennas (the transmitting and the receiving) are mounted on high towers or buildings.
- The terrain beneath is smooth.
- The source antenna has very low side lobes so that practically there is no energy directed toward the surface below (the ground) or the buildings behind.
- The line-of-sight is always clear.

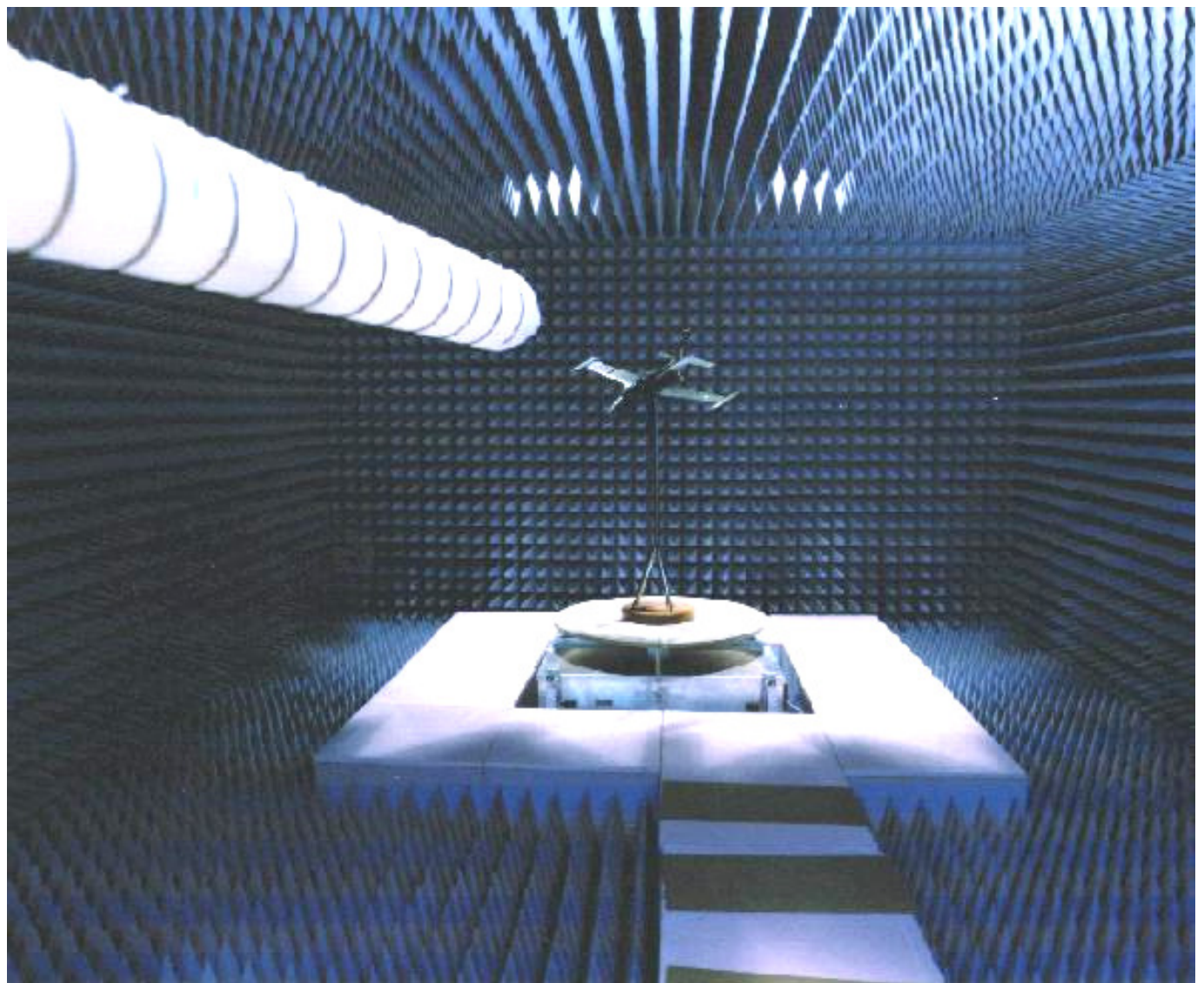


The slant ranges need less space than the elevated ranges. The test antenna is mounted at a fixed height on a non-conducting tower (e.g. made of fiber glass), while the source antenna is mounted near the ground. The source antenna must have its pattern null pointed toward ground. It is desirable that it has very low side lobes and narrow beamwidth. Slant ranges still require wide open space to minimize reflections from surrounding buildings.



The anechoic chambers are the most popular antenna measurement sites especially in the microwave frequency range. They provide convenience and controlled EM environment. However, they are expensive to build and maintain. An anechoic chamber is a large room, the walls, floor and ceiling of which are lined with steel sheets. In effect, an anechoic chamber is a huge Faraday cage, which provides near ideal protection against external EM noise and interference. In addition, all inner surfaces of the chamber are lined with RF/microwave absorbers. An anechoic chamber is shown in the photo below. A comprehensive description of the EM anechoic chambers can be found in

L.H. Hemming, *Electromagnetic Anechoic Chambers: A Fundamental Design and Specifications Guide*, IEEE Press/Wiley, 2002.

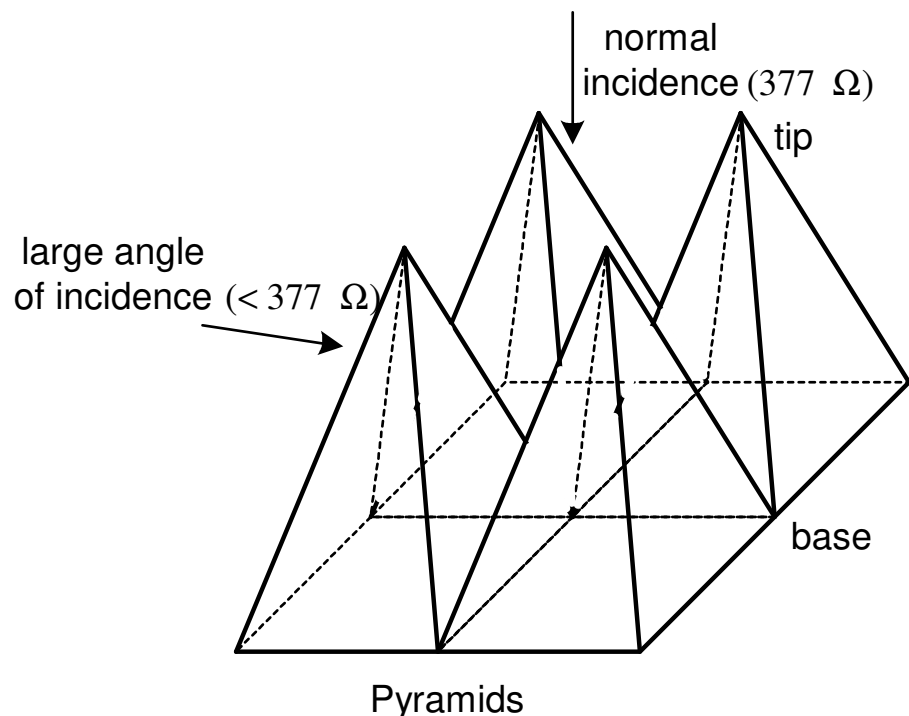


The first EM wave absorbers were developed during World War II in both US and German laboratories. The manufacturing of anechoic chambers became possible after RF/microwave absorbing materials with improved characteristics had become commercially available. The first broadband absorbers were made of a material called *hairflex* consisting of animal fibres sprayed with (or dipped in) conducting carbon in neoprene. A historical summary of the development of EM wave absorbing materials is given by Emerson in his paper:

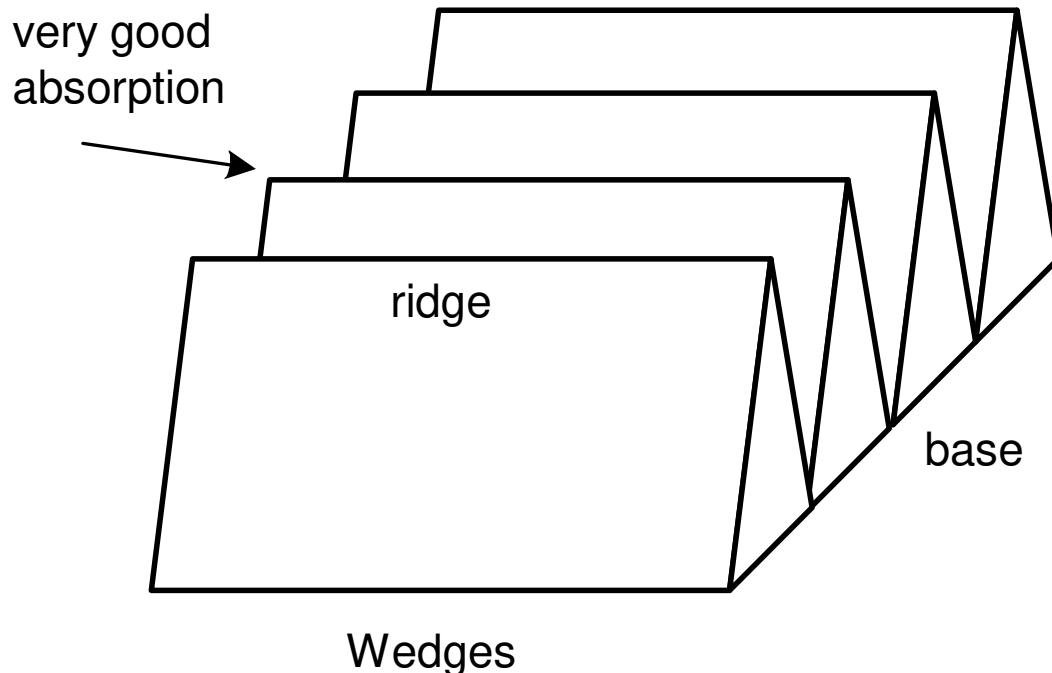
W.H. Emerson, “Electromagnetic wave absorbers and anechoic chambers through the years,” *IEEE Trans. on Antennas and Propagation*, vol. AP-21, pp. 484-489, July 1973.

Nowadays, absorbing elements are with much improved characteristics providing reflection coefficients as low as -50 dB at normal incidence. Reflection increases as the angle of incidence increases. For example, a typical reflection of -25 dB is related to an angle of incidence of about 70 degrees.

A typical absorbing element has the form of a pyramid or a wedge. Pyramids are designed to absorb the waves at normal (nose-on) incidence best. They do not perform well at large angles of incidence. They act, in effect, as a tapered impedance transition for normal incidence of the EM wave from the intrinsic impedance of 377Ω to the short of the chamber’s wall. Their resistance gradually decreases as the pyramid’s cross-section increases.



Wedges, on the other hand, perform much better than pyramids for waves, which travel nearly parallel to their ridges.

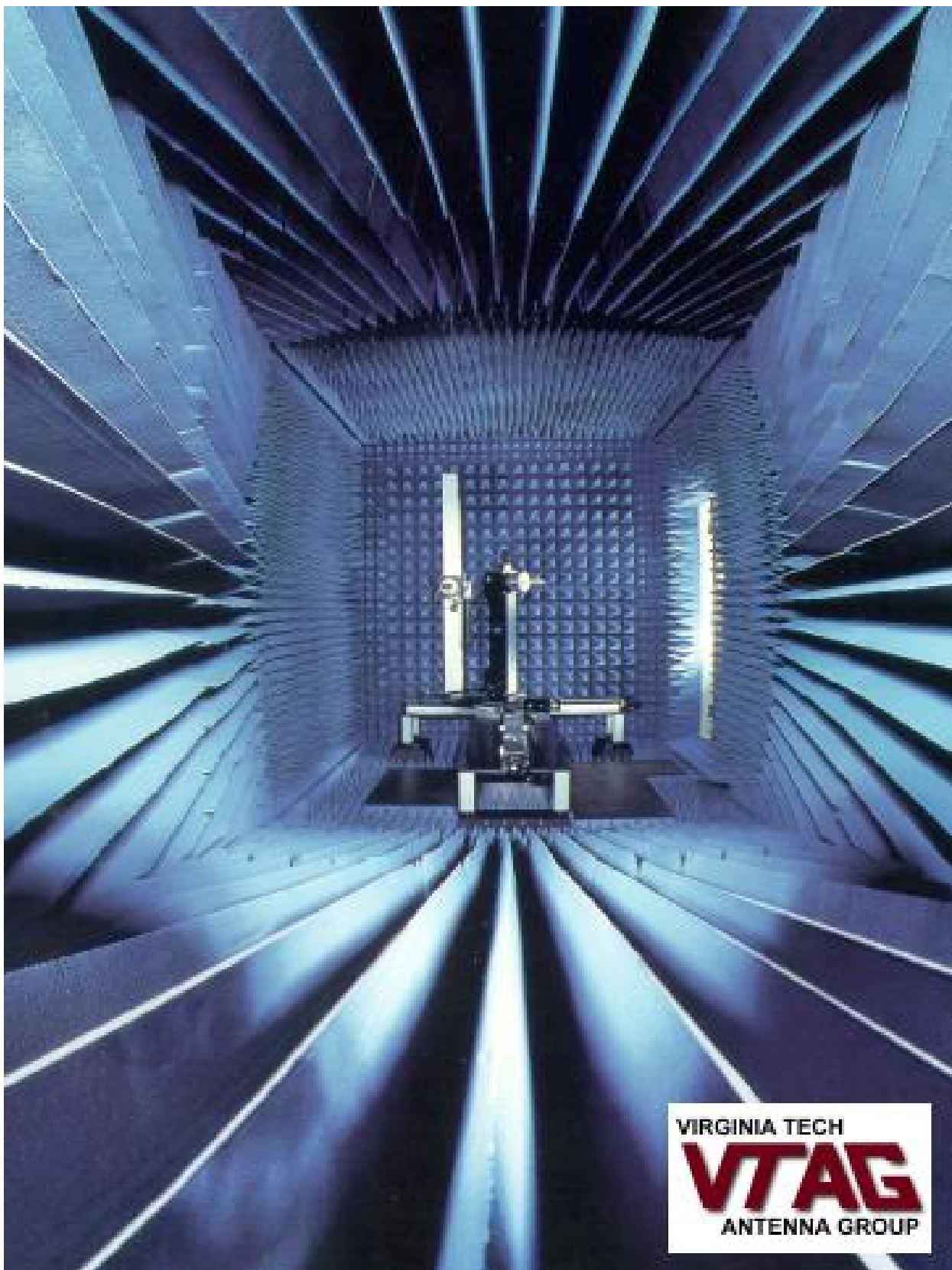


For more detailed information on absorbing materials and shapes see:

John Kraus, *Antennas*, 2nd edition, McGraw-Hill, Inc.

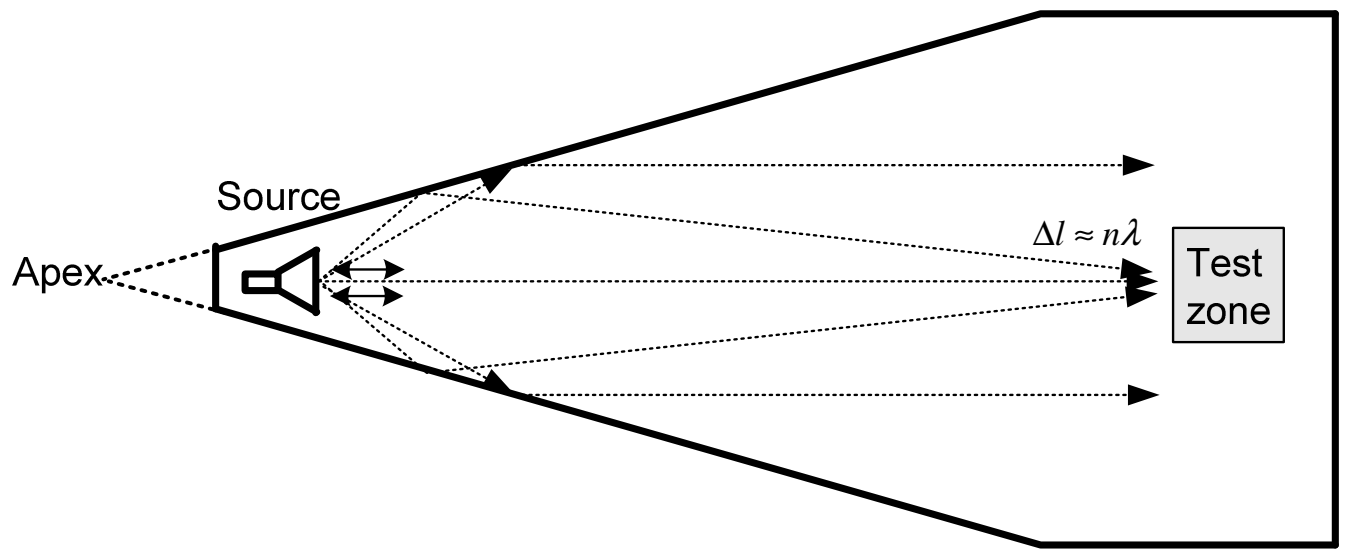
B.T. DeWitt and W.D. Burnside, “Electromagnetic scattering by pyramidal and wedge absorber,” *IEEE Trans. on Antennas and Propagation*, 1988.

An anechoic chamber lined with both types of absorbing shapes is shown below.



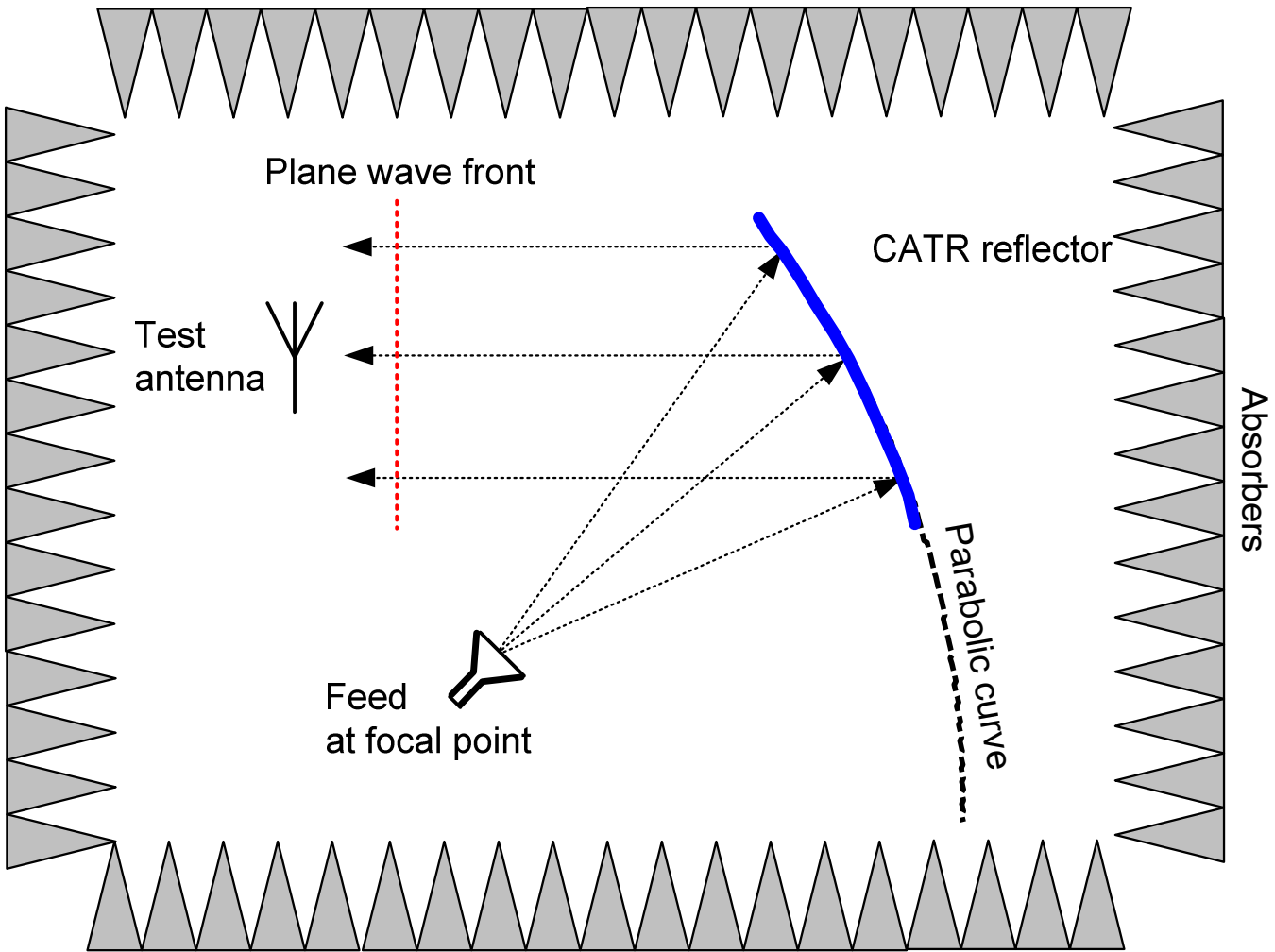
VIRGINIA TECH
VTAG
ANTENNA GROUP

There are two types of anechoic chambers: rectangular and tapered. The design of both chamber types is based on the principles of geometrical optics. The goal is to minimize the amplitude and phase ripples in the test zone (the quiet zone), which are due to the imperfect absorption by the wall lining. The tapered chamber has the advantage of tuning by moving the source antenna closer to (at higher frequencies) or further from (at lower frequencies) the apex of the taper. Thus, the reflected rays are adjusted to produce nearly constructive interference with the direct rays at the test location.



Anechoic chambers are limited by the distance requirements of the far-field measurements of large antennas or scatterers. There are two basic approaches to overcome this limitation. One is presented by the *Compact Antenna Test Ranges (CATRs)*, which produce a nearly uniform plane wave in a very short distance via a system of reflectors (or a single paraboloidal reflector). Another approach is based on near-to-far field transformation, where the measurements are performed in the near-field zone or in the Fresnel zone of the AUT.

The CATR utilizes a precision paraboloidal antenna to collimate the energy of a primary feed antenna in a short distance. Typical arrangement of a compact range is shown below.



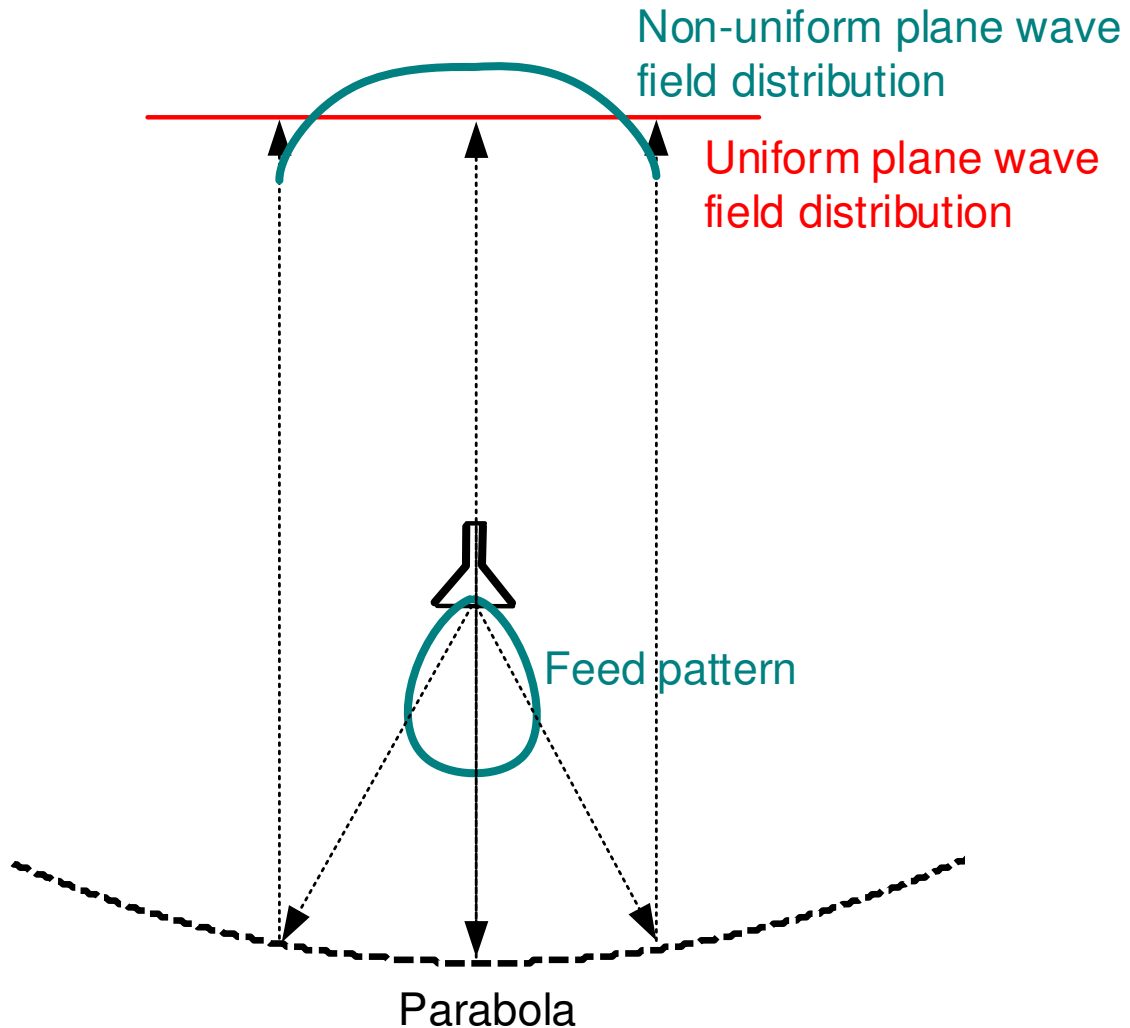
The linear dimensions of the reflector must be at least three to four times those of the AUT so that its illumination is sufficiently close to a uniform plane wave. An offset feed is used for the reflector to prevent aperture blockage and to reduce the diffraction from the primary feed structure. The paraboloidal reflector surface must be fabricated with high precision to obtain fairly uniform amplitude distribution of the incident field at the test antenna.

A perfect plane wave is produced by the CATR if the paraboloidal reflector has a perfect surface, infinite size, and if the feed is a point source with a pattern which compensates for the space attenuation. Of course, such ideal conditions cannot be achieved, and the field distribution in a real CATR deviates from the uniform plane wave. However, it is within acceptable parameters in the quite zone.

The quiet zone is typically 50% to 60% the aperture of the reflector. The imperfections of the field in the quiet zone are measured in terms of *phase*

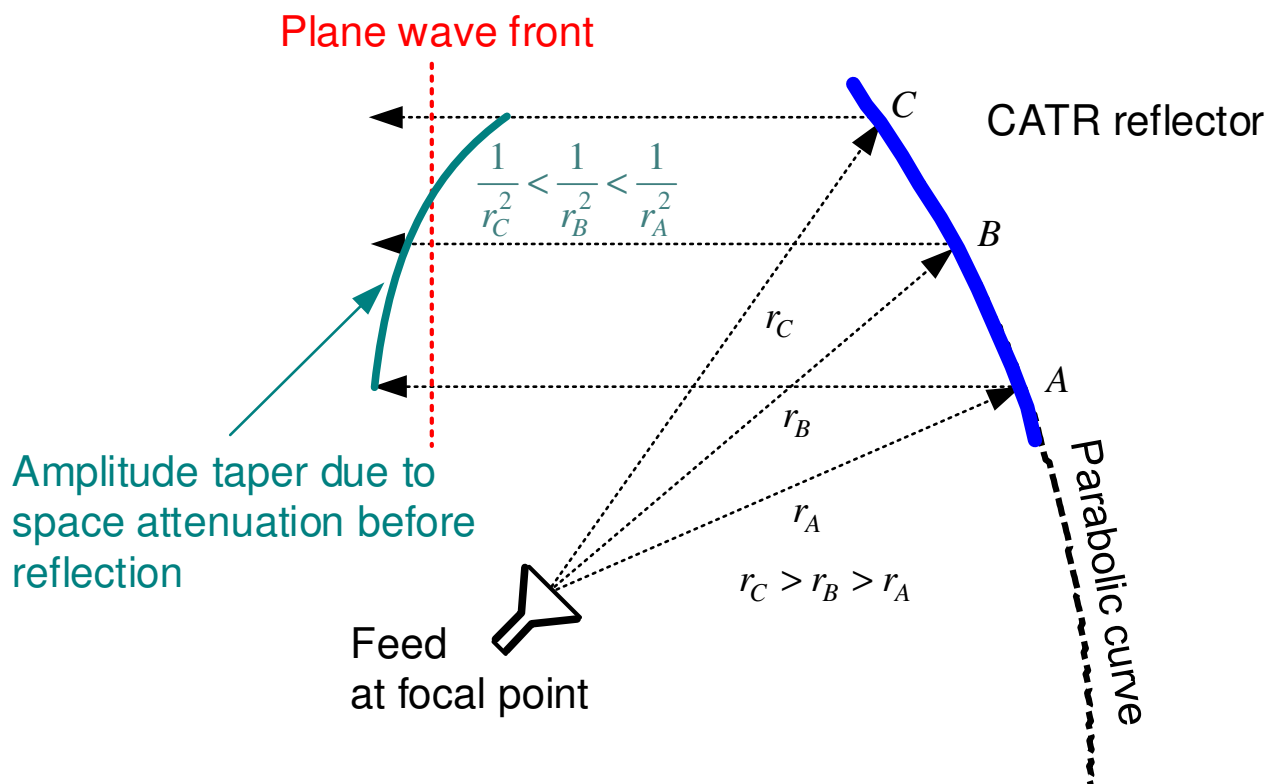
errors, ripple-amplitude deviations, and taper-amplitude deviations. Acceptable deviations for most CATRs are: less than 10% phase error, less than 1 dB ripple and taper amplitude deviations.

Amplitude taper in the quiet zone is due to two reasons: the primary feed pattern and the space attenuation. The primary feed cannot be isotropic; therefore, its pattern has variations with direction. Usually, the pattern gradually decreases as the directional angles point away from the antenna axis. This is called feed-amplitude taper. That portion of the feed pattern, which illuminates the CATR surface, is directly transferred into the quiet zone, thus contributing to the field amplitude-taper deviation from the ideal uniform plane wave.

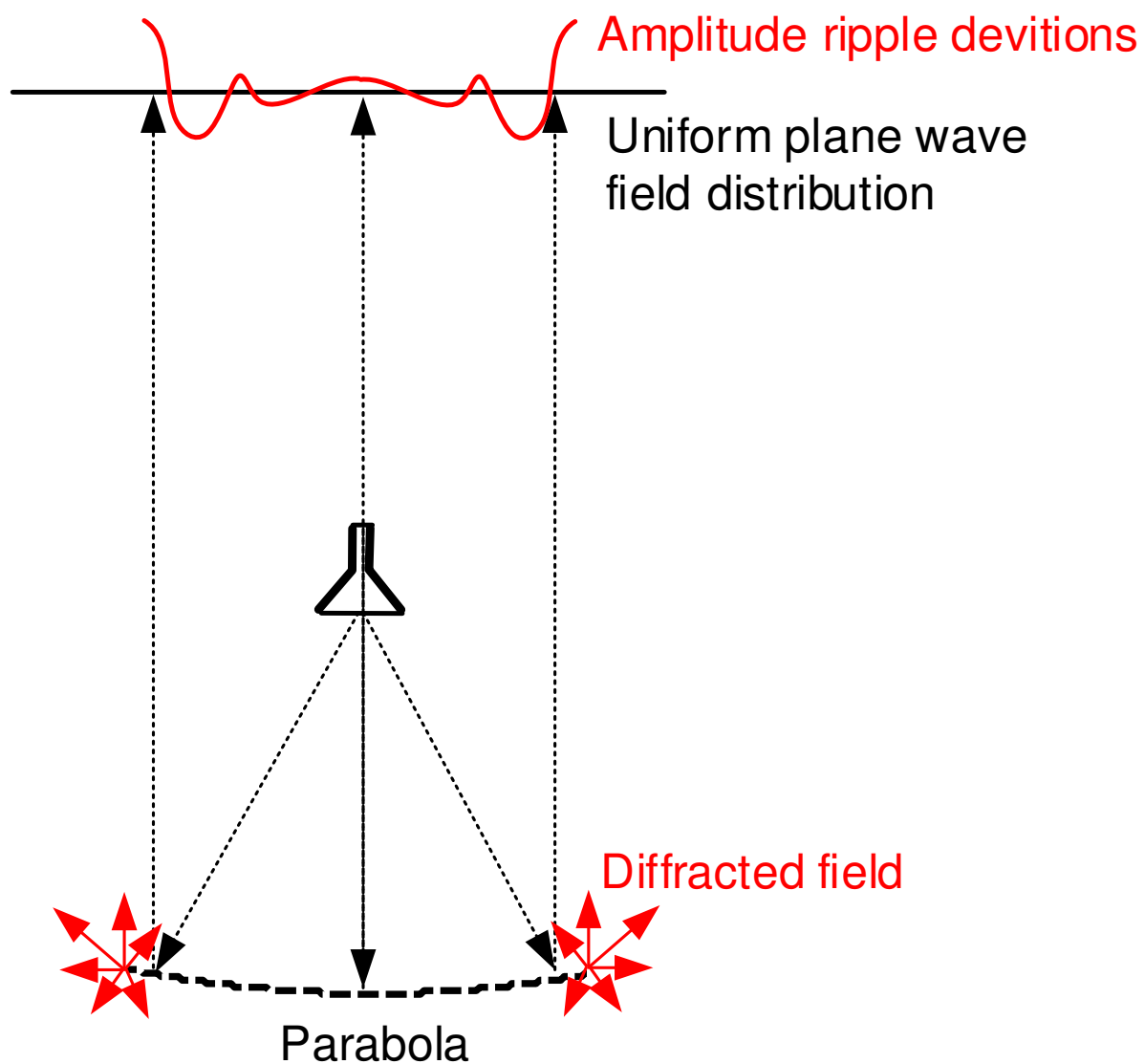


It is obvious that if the feed pattern is nearly isotropic for the angles illuminating the reflector, the feed-amplitude taper will be very small. That is why low-directivity antennas are preferred as feeds. However, the feed cannot be omnidirectional because direct illumination of the AUT by the primary feed is unacceptable. The careful choice of the feed antenna and its location is of paramount importance for the CATR design.

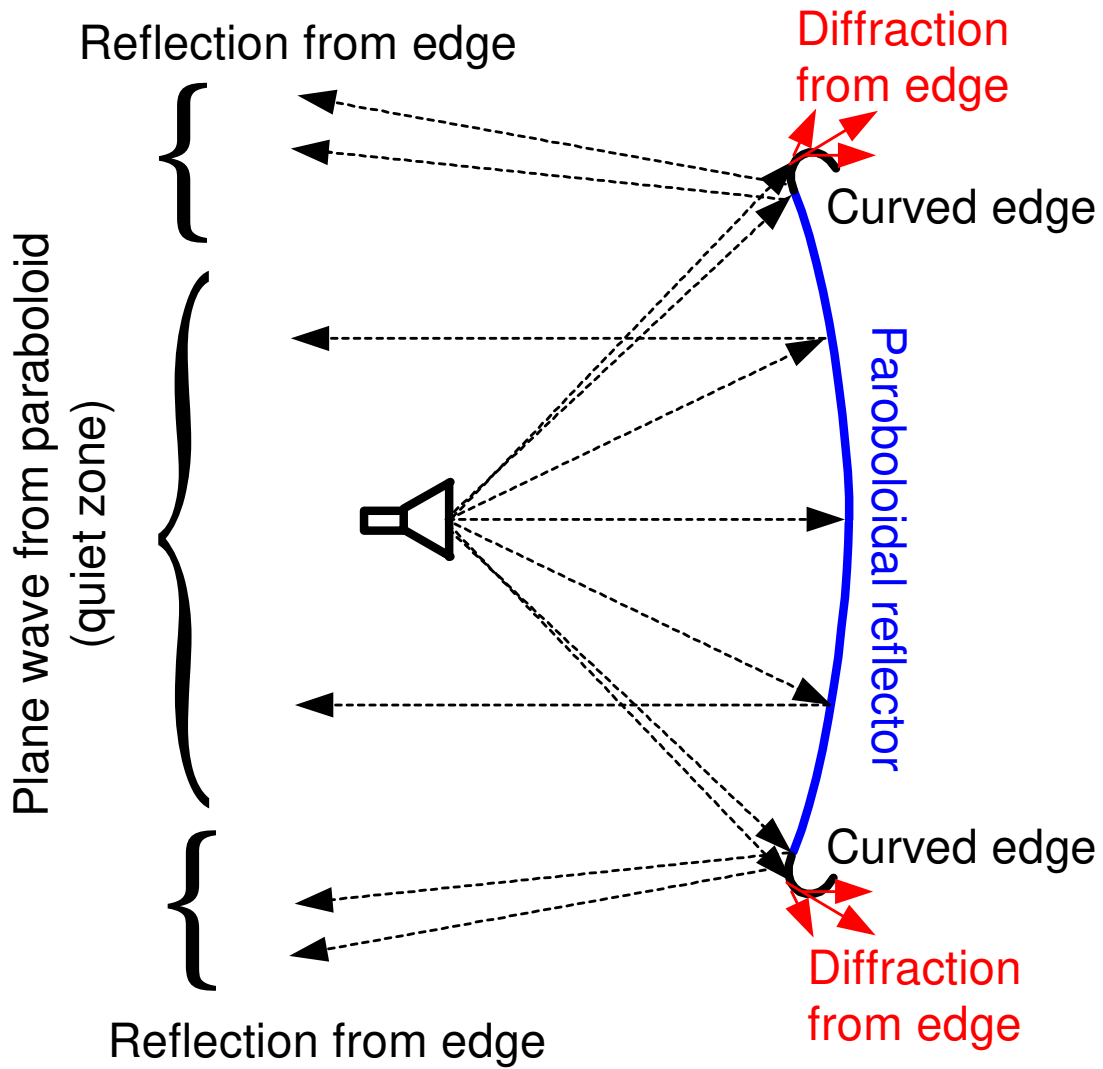
The $1/r^2$ power space attenuation occurs with the spherical spreading of the uncollimated energy radiated by the primary feed toward the reflector. The paths of these primary EM rays from the feed to the reflector are of different lengths, which results in different amplitude across the front of the reflected collimated EM wave. This is yet another reason for amplitude taper deviations in the quiet zone.



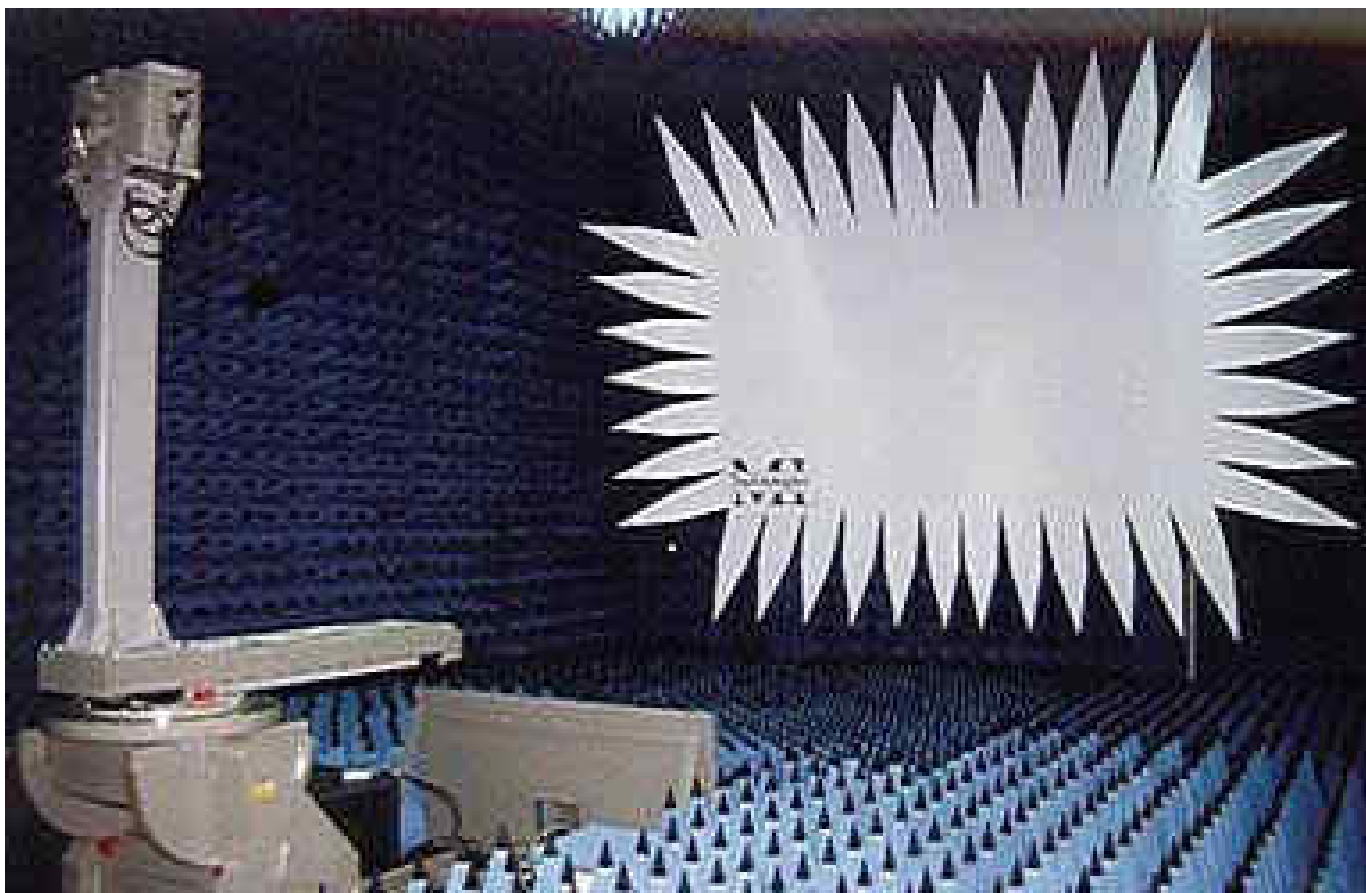
Amplitude and phase ripples in the quiet zone are primarily caused by diffraction from the edges of the reflector. The diffracted field is spread in all directions interfering with the major reflected field in constructive and destructive patterns. The result is the appearance of maxima and minima of the field amplitude across the plane wave front in the quiet zone. Diffraction from edges causes deviation of the phase of the plane wave, too.



There are two common ways to reduce diffraction from reflector edges: serrated-edge reflectors and rolled-edge reflectors. Rolled-edge modifications at the edge of the reflector are introduced to direct the diffracted field mainly to the side and the back of the reflector.



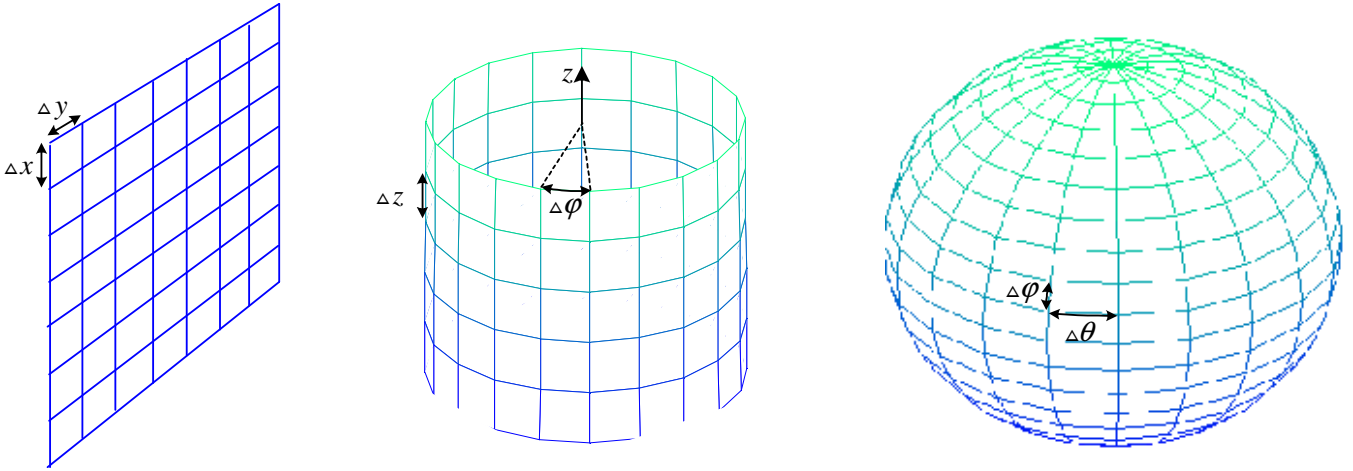
Serrated edges of reflectors produce multiple low-amplitude diffractions, which are randomized in amplitude, phase and polarization. That is why the probability of their cancellation in any point of the quiet zone is high. Serrations are typically of irregular triangular shape. To further reduce the diffraction in the direction of the test zone, the serrated edges may be also rolled backwards. A photograph of a compact range whose reflector has serrated edges is shown below.



4. Near-to-far Field Transformations for Compact Ranges

Another approach for measuring far-field patterns, which allows for the most compact chambers, is the near-field/far-field (NF/FF) method. The field amplitude, phase and polarization are measured in the near field of the AUT, which is in radiating mode. The near-field data is transformed to far-field patterns via analytical techniques implemented in the sophisticated software run by an automated computer system, which controls the measurement procedure.

The magnitude and phase of the tangential \mathbf{E} field are measured at regular intervals over a canonical surface (plane, cylinder, or sphere) located close to the AUT. The sampled \mathbf{E} field is used to calculate the angular spectrum of the plane, the cylindrical or the spherical wave. This spectrum matches closely the radiated field angular distribution. This is called ***modal expansion*** of the radiated field.



Here, we consider the simplest data acquisition over a planar surface and its modal expansion. We show that ***the far-field radiation pattern of any aperture (surface) is the Fourier transform of the aperture field distribution***. We next derive the formulas in the case of a planar acquisition aperture.

Assume that in the near-field measurements, the \mathbf{E} vector is measured over a planar surface, which is our aperture. According to the ***equivalence principle***, we can now assume that the field behind the surface (on the side of the antenna) is equal to zero, and its impact on the field on the other side of the surface is due to equivalent surface currents:

$$\begin{aligned}\mathbf{J}_s &= \hat{\mathbf{n}} \times \mathbf{H}_a \\ \mathbf{M}_s &= -\mathbf{n} \times \mathbf{E}_a.\end{aligned}\tag{9}$$

Here, \mathbf{E}_a and \mathbf{H}_a represent the field vectors at the aperture (the surface) due to the antenna behind it. \mathbf{J}_s is the equivalent electric surface current density, \mathbf{M}_s is the equivalent magnetic surface current density, and $\hat{\mathbf{n}}$ is the surface unit normal pointing toward the region of observation (away from the antenna).

Since the field behind the planar surface is now set to zero, we can as well assume that the medium behind the surface is a perfect conductor. In the case of a flat surface of size much larger than a wavelength, the image theory can be applied. Now the equivalent surface sources become

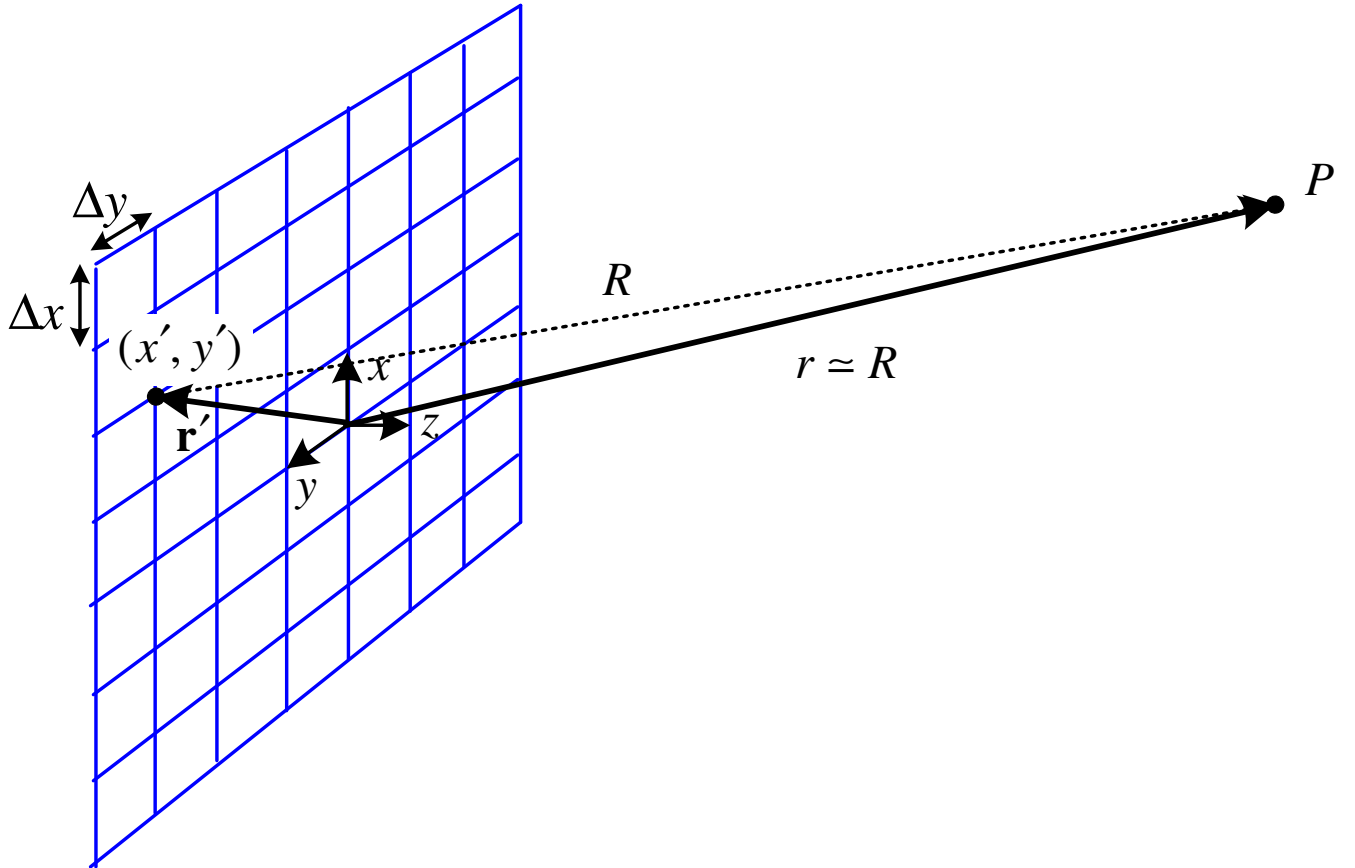
$$\mathbf{J}_s = 0; \quad \mathbf{M}_s = -\hat{\mathbf{n}} \times (2\mathbf{E}_a).\tag{10}$$

The equivalent surface magnetic currents \mathbf{M}_s create an electric vector

potential \mathbf{F} , which, in the far zone, is

$$\mathbf{F}(P) \approx -\varepsilon \frac{e^{-j\beta r}}{4\pi r} \hat{\mathbf{n}} \times \iint_{S_a} 2\mathbf{E}_a(\mathbf{r}') e^{j\mathbf{k} \cdot \mathbf{r}'} d\mathbf{s}' = -\varepsilon \frac{e^{-j\beta r}}{2\pi r} \hat{\mathbf{n}} \times \iint_{S_a} \mathbf{E}_a(\mathbf{r}') e^{j\mathbf{k} \cdot \mathbf{r}'} d\mathbf{s}' \quad (11)$$

where $\beta = \omega\sqrt{\mu\varepsilon}$ is the wavenumber, $\mathbf{r}' = \hat{\mathbf{x}}x' + \hat{\mathbf{y}}y'$ is the position vector of the integration point, and r is the distance from the observation point P to the origin.



Note that the far-field approximations have been applied to the amplitude and phase terms of the vector-potential integral. The propagation vector $\mathbf{k} = \beta\hat{\mathbf{r}}$ shows the direction of propagation and has a magnitude equal to the wave number β . The scalar product $\mathbf{k} \cdot \mathbf{r}' = \beta r' \hat{\mathbf{r}} \cdot \hat{\mathbf{r}'}$ yields the familiar phase term accounting for the phase delay associated with the source point location.

We now remember that the far-field \mathbf{E} vector is related to the far-field vector potential \mathbf{F} as

$$\mathbf{E}^{\text{far}} = -j\omega\eta\mathbf{F} \times \hat{\mathbf{r}}. \quad (12)$$

Here, $\eta = \sqrt{\mu/\epsilon}$ is the intrinsic impedance of the medium. Substituting (11) in (12) yields:

$$\mathbf{E}^{\text{far}} \approx -j\beta \frac{e^{-j\beta r}}{2\pi r} \hat{\mathbf{r}} \times \iint_{S_a} (\hat{\mathbf{n}} \times \mathbf{E}_a) e^{j\mathbf{k} \cdot \mathbf{r}'} dx' dy'. \quad (13)$$

In the case of a planar surface, the unit normal is constant, and we can assume that $\hat{\mathbf{n}} = \hat{\mathbf{z}}$. Having in mind that the rectangular components of the radial unit vector are

$$\hat{\mathbf{r}} = \hat{\mathbf{x}} \sin \theta \cos \varphi + \hat{\mathbf{y}} \sin \theta \sin \varphi + \hat{\mathbf{z}} \cos \theta, \quad (14)$$

we can calculate the x and y components of \mathbf{E}^{far} as

$$E_x^{\text{far}} \approx j\beta \frac{e^{-j\beta r}}{2\pi r} \cdot \cos \theta \cdot \iint_{S_a} E_{xa}(x', y') e^{j(k_x x' + k_y y')} dx' dy', \quad (15)$$

$$E_y^{\text{far}} \approx j\beta \frac{e^{-j\beta r}}{2\pi r} \cdot \cos \theta \cdot \iint_{S_a} E_{ya}(x', y') e^{j(k_x x' + k_y y')} dx' dy'. \quad (16)$$

Here, k_x and k_y are the spectral variables, which are the components of the propagation vector \mathbf{k} in the xy plane:

$$\begin{aligned} k_x &= \beta \sin \theta \cos \varphi, \\ k_y &= \beta \sin \theta \sin \varphi. \end{aligned} \quad (17)$$

The z -component of the far \mathbf{E} field is found as

$$\begin{aligned} E_z^{\text{far}} &\approx -j\beta \frac{e^{-j\beta r}}{2\pi r} \cdot \sin \theta \cdot \\ &\left[\cos \varphi \iint_{S_a} E_{xa}(x', y') e^{j(k_x x' + k_y y')} dx' dy' + \sin \varphi \iint_{S_a} E_{ya}(x', y') e^{j(k_x x' + k_y y')} dx' dy' \right]. \end{aligned} \quad (18)$$

It is obvious from (15), (16) and (18) that if the components E_x^{far} and E_y^{far} are known, the E_z^{far} component can be calculated (if need be) as

$$E_z^{\text{far}} = -\tan \theta \cdot [E_x^{\text{far}} \cos \varphi + E_y^{\text{far}} \sin \varphi]. \quad (19)$$

Let us examine the integrals appearing in (15) and (16):

$$f_x(k_x, k_y) = \iint_{S_a} E_{xa}(x', y') e^{j(k_x x' + k_y y')} dx' dy', \quad (20)$$

$$f_y(k_x, k_y) = \iint_{S_a} E_{ya}(x', y') e^{j(k_x x' + k_y y')} dx' dy'. \quad (21)$$

These integrals are the 2-D Fourier transforms of the tangential field distribution, $E_{xa}(-x', -y')$ and $E_{ya}(-x', -y')$, over the area of the surface S_a . The surface is ideally infinite ($-\infty < x' < +\infty$, $-\infty < y' < +\infty$). In practice, the surface where the field is measured is finite and designed so that the field components outside of it are negligible. The functions f_x and f_y depend on the spectral variables k_x and k_y .

Note that the functions $f_x(k_x, k_y)$ and $f_y(k_x, k_y)$ give the far-field pattern in terms of the field x and y components for small θ when $\cos \theta \approx 1$:

$$\left. \begin{array}{l} \bar{E}_x^{\text{far}}(\theta, \varphi) \approx f_x(k_x, k_y) \\ \bar{E}_y^{\text{far}}(\theta, \varphi) \approx f_y(k_x, k_y) \end{array} \right\} \text{for } \cos \theta \approx 1, \text{ where } \begin{cases} k_x = \beta \sin \theta \cos \varphi, \\ k_y = \beta \sin \theta \sin \varphi. \end{cases} \quad (22)$$

This finally clarifies the statement that ***the far-field pattern is the Fourier transform of the aperture field distribution.***

The far-field z -component can be expressed by its spectral counterpart $f_z(k_x, k_y)$ in the same manner as the x and y components:

$$E_z^{\text{far}} = jk \frac{e^{-jkr}}{r} \cdot \cos \theta \cdot f_z(k_x, k_y). \quad (23)$$

Having in mind (18) and (19), it becomes clear that $f_z(k_x, k_y)$ is not an independent function but is related to the other two spectral components as

$$f_z(k_x, k_y) = -\tan \theta \cdot [f_x(k_x, k_y) \cos \varphi + f_y(k_x, k_y) \sin \varphi]. \quad (24)$$

We can now define the vector plane-wave spectral function:

$$\mathbf{f}(k_x, k_y) = \hat{\mathbf{x}} f_x(k_x, k_y) + \hat{\mathbf{y}} f_y(k_x, k_y) + \hat{\mathbf{z}} f_z(k_x, k_y) \quad (25)$$

the spatial components of which are calculated via (20), (21) and (24). The far-field \mathbf{E} vector can be calculated from the spectral function as

$$\mathbf{E}(r, \theta, \varphi) \approx j\beta \frac{e^{-j\beta r}}{2\pi r} \cos \theta \cdot \mathbf{f}(k_x, k_y). \quad (26)$$

We can express the vector equation (26) in terms of the θ and φ components of the far-field \mathbf{E} vector:

$$\begin{aligned} E_\theta(r, \theta, \varphi) &\approx j\beta \frac{e^{-j\beta r}}{2\pi r} \cos\theta \cdot f_\theta(k_x, k_y), \\ E_\varphi(r, \theta, \varphi) &\approx j\beta \frac{e^{-j\beta r}}{2\pi r} \cos\theta \cdot f_\varphi(k_x, k_y). \end{aligned} \quad (27)$$

Since the spectral function \mathbf{f} is derived via its rectangular components during the data acquisition over a planar surface, it is desirable to convert f_θ and f_φ to f_x and f_y . Following the standard transformation from spherical to rectangular components, we obtain

$$\cos\theta \cdot f_\theta = \cos\theta(f_x \cos\theta \cos\varphi + f_y \cos\theta \sin\varphi - f_z \sin\theta). \quad (28)$$

After substituting f_z from (24), we arrive at

$$\cos\theta \cdot f_\theta = f_x \cos\varphi + f_y \sin\varphi. \quad (29)$$

In analogous manner, it can be shown that

$$\cos\theta \cdot f_\varphi = -f_x \sin\varphi + f_y \cos\varphi. \quad (30)$$

The substitution of (29) and (30) into (27) finally gives

$$\begin{aligned} E_\theta(r, \theta, \varphi) &\approx jk \frac{e^{-jkr}}{2\pi r} (f_x \cos\varphi + f_y \sin\varphi) \\ E_\varphi(r, \theta, \varphi) &\approx jk \frac{e^{-jkr}}{2\pi r} (-f_x \sin\varphi + f_y \cos\varphi). \end{aligned} \quad (31)$$

We can now summarize the procedure of the NF/FF pattern measurement in three basic steps:

- Measure the tangential \mathbf{E} field components $E_{xa}(x', y', z' = 0)$ and $E_{ya}(x', y', z' = 0)$ over the near-field aperture (data acquisition).
- Calculate the plane-wave spectral functions $f_x(k_x, k_y)$ and $f_y(k_x, k_y)$ using (20) and (21).
- Calculate the normalized far-field components using

$$\begin{aligned} \bar{E}_\theta(\theta, \varphi) &= f_x \cos\varphi + f_y \sin\varphi, \\ \bar{E}_\varphi(\theta, \varphi) &= -f_x \sin\varphi + f_y \cos\varphi, \end{aligned} \quad (32)$$

and the total normalized field pattern using

$$\bar{E}(\theta, \varphi) = \sqrt{\bar{E}_\theta^2(\theta, \varphi) + \bar{E}_\varphi^2(\theta, \varphi)} = \sqrt{f_x^2(k_x, k_y) + f_y^2(k_x, k_y)}. \quad (33)$$

In the actual test procedure, a planar surface is chosen a distance z_0 away from the test antenna, which is in radiating mode. This surface is called the *measurement aperture*. The distance z_0 is at least three wavelengths away from the antenna, so that the measurement is carried out in the radiating near-field region (Fresnel zone) rather than in the reactive near-field region where the amplitude and phase variations of the field are too rapid and the sampling intervals must be very small.

The measurement aperture is rectangular of dimensions $a \times b$. It is divided into $M \times N$ points spaced evenly Δx and Δy apart. The relation between the number of points and the respective spacing is then

$$M = \frac{a}{\Delta x} + 1, \quad N = \frac{b}{\Delta y} + 1. \quad (34)$$

Thus, the sampling points are located at coordinates $(m\Delta x, n\Delta y, 0)$ where $0 \leq m \leq M - 1$ and $0 \leq n \leq N - 1$. The separation distances Δx and Δy must be less than half a wavelength in order to satisfy Nyquist's sampling criterion and such that the equations in (34) yield integer numbers. The measurement aperture must be large enough so that the signal at its edges is at least 45 dB down from the maximum measured signal on the acquisition surface.

The plane-wave spectral function $\mathbf{f}(k_x, k_y)$ can be evaluated at a discrete set of wave numbers as dictated by the discrete Fourier transform:

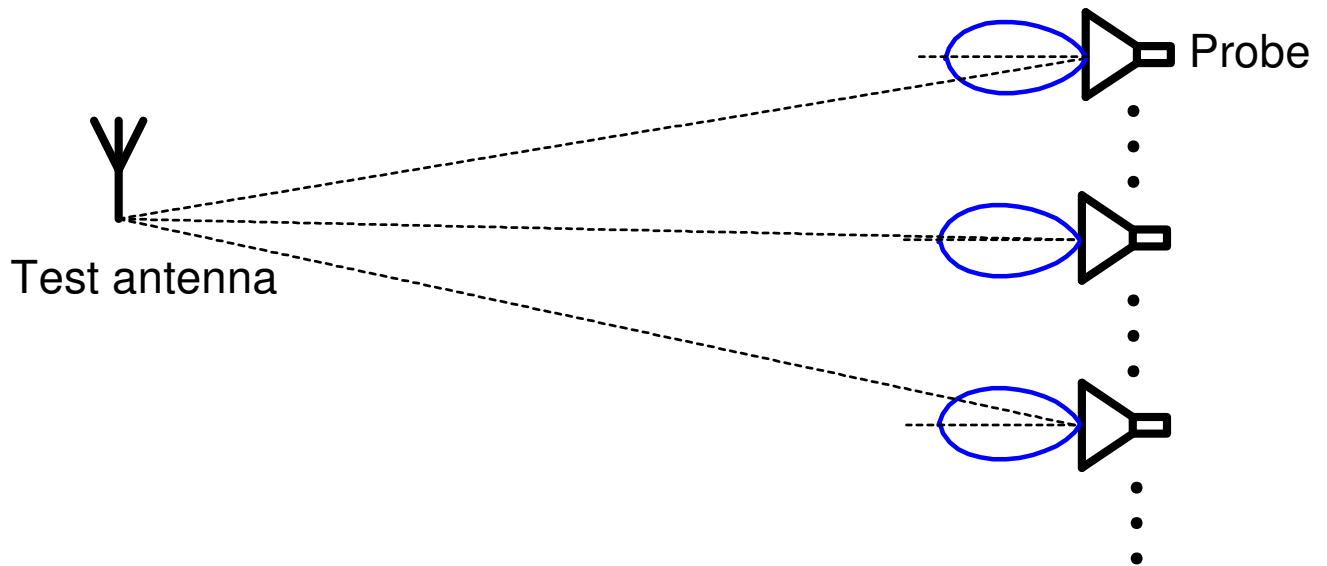
$$\begin{aligned} k_x &= m \frac{2\pi}{a} = m \underbrace{\frac{2\pi}{(M-1)\Delta x}}_{\Delta k_x} \\ k_y &= n \frac{2\pi}{b} = n \underbrace{\frac{2\pi}{(N-1)\Delta x}}_{\Delta k_y}. \end{aligned} \quad (35)$$

Conventional two-dimensional FFT (Fast Fourier Transform) techniques are used to perform this transformation.

The acquisition of the planar near-field data is done by a computer-controlled probe antenna (typically a waveguide horn or an open waveguide),

which is moved to each grid node over the measurement aperture by a high-precision positioning system (positioner). The probe's axis is held stationary and normal to the measurement aperture. The probe must be linearly polarized so that separate measurements of the two tangential field components E_x and E_y become possible.

As the probe location changes, its pattern orientation with respect to the AUT changes, too, as shown below. The probe's partial directivities in the direction of the test antenna must be taken into account using probe compensation techniques.



The principal advantage of the planar NF/FF transformation over the cylindrical and the spherical one is its mathematical simplicity. Its major disadvantage is that it cannot cover all directional angles. In the ideal case of infinite planar measurement surface, only one hemisphere of the antenna pattern can be measured. Thus, the back lobes and the side lobes of the antenna cannot be measured together with the main beam. Of course, the AUT can be rotated in different positions, so that the overall pattern can be reconstructed.

The reader interested in the subject of NF/FF transforms and measurements is referred to the following introductory sources:

R.C. Johnson, H.A. Ecker, and J.S. Hollis, "Determination of far-field antenna patterns from near-field measurements," *Proc. IEEE*, vol. 61, No. 12, pp. 1668-1694, Dec. 1973.

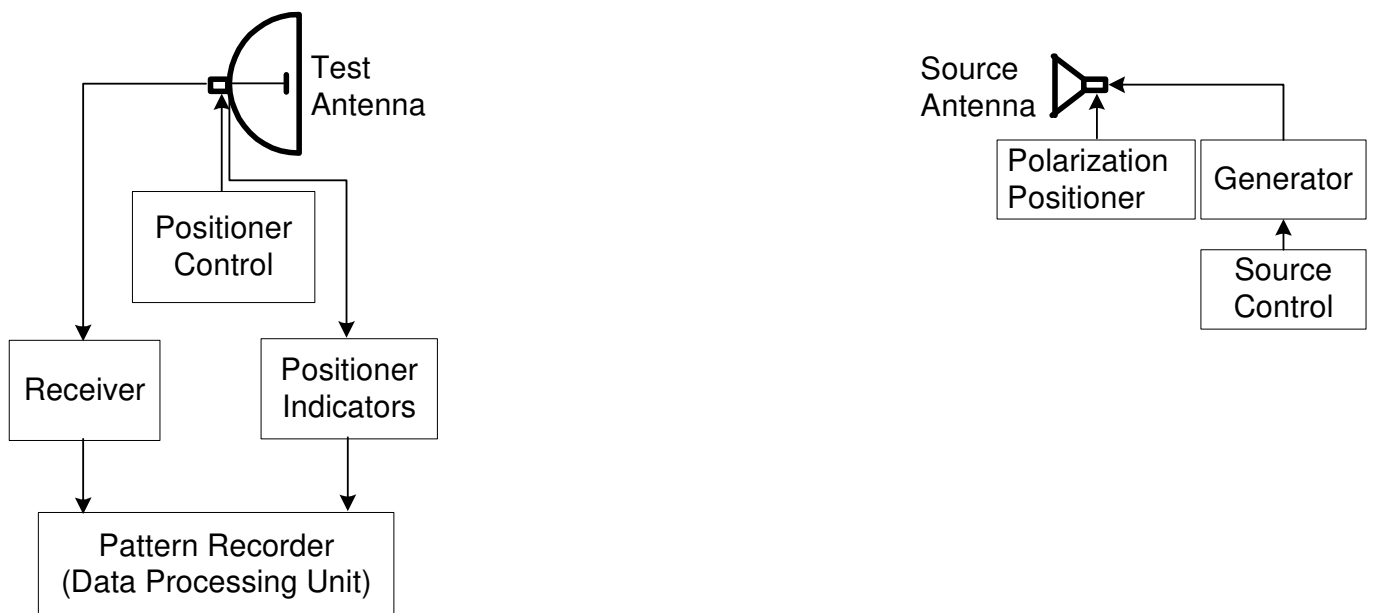
D.T. Paris, W.M. Leach, Jr., and E.B. Joy, "Basic theory of probe compensated near-field measurements," *IEEE Trans. on Antennas and Propagation*, vol. AP-26, No. 3, pp. 373-379, May 1978.

E.B. Joy, W.M. Leach, Jr., G.P. Rodrigue, and D.T. Paris, "Applications of probe compensated near-field measurements," *IEEE Trans. on Antennas and Propagation*, vol. AP-26, No. 3, pp. 379-389, May 1978.

A.D. Yaghjian, "An overview of near-field antenna measurements," *IEEE Trans. on Antennas and Propagation*, vol. AP-34, pp. 30-45, January 1986.

5. Far-field Pattern Measurements*

The far-field patterns are measured on the surface of a sphere of constant radius. Any position on the sphere is identified by the directional angles θ and φ of the spherical coordinate system. In general, the pattern of an antenna is 3-D. However, 3-D pattern acquisition is difficult – it involves multiple 2-D pattern measurements. The minimal number of 2-D patterns is two, and these two patterns must be in two orthogonal principal planes. A principal plane must contain the direction of maximum radiation. A simplified block diagram of a pattern measurement system is given below.



The total ***amplitude pattern*** is described by the vector sum of the two orthogonally polarized radiated field components:

$$|\mathbf{E}| = \sqrt{|E_\theta|^2 + |E_\varphi|^2}. \quad (36)$$

Rarely, the separate patterns for both components are needed. This is the case when the polarization of the test antenna must be characterized in addition to its pattern.

For antennas of low directivity, at least three 2-D pattern cuts are necessary in order to obtain good 3-D pattern approximation: in the two elevation planes at $\varphi = 0^\circ / 180^\circ$ and $\varphi = 90^\circ / 270^\circ$ as well as the azimuth pattern at $\theta = 90^\circ$.

For high-directivity antennas, only two orthogonal 2-D elevation patterns often suffice. Assuming that the antenna boresight is along the z -axis, these are the patterns at $\varphi = 0^\circ / 180^\circ$ and $\varphi = 90^\circ / 270^\circ$. The 3-D pattern approximation from 2-D patterns is discussed below.

High-directivity aperture antennas such as horn and reflector antennas can have their far-field components expressed as

$$E_\theta(\theta, \varphi) = j\beta \frac{e^{-j\beta r}}{4\pi r} \left[\mathcal{J}_x^E \cos \varphi + \mathcal{J}_y^E \sin \varphi + \eta \cos \theta (\mathcal{J}_y^H \cos \varphi - \mathcal{J}_x^H \sin \varphi) \right], \quad (37)$$

$$E_\varphi(\theta, \varphi) = j\beta \frac{e^{-j\beta r}}{4\pi r} \left[-\eta (\mathcal{J}_x^H \cos \varphi + \mathcal{J}_y^H \sin \varphi) + \cos \theta (\mathcal{J}_y^E \cos \varphi - \mathcal{J}_x^E \sin \varphi) \right]. \quad (38)$$

Here, \mathcal{J}_x^E , \mathcal{J}_y^E , \mathcal{J}_x^H and \mathcal{J}_y^H are the plane-wave spectral functions:

$$\mathcal{J}_x^E(\theta, \varphi) = \iint_{S_A} E_{ax}(x', y') e^{j\beta(x' \sin \theta \cos \varphi + y' \sin \theta \sin \varphi)} dx' dy', \quad (39)$$

$$\mathcal{J}_y^E(\theta, \varphi) = \iint_{S_A} E_{ay}(x', y') e^{j\beta(x' \sin \theta \cos \varphi + y' \sin \theta \sin \varphi)} dx' dy', \quad (40)$$

$$\mathcal{J}_x^H(\theta, \varphi) = \iint_{S_A} H_{ax}(x', y') e^{j\beta(x' \sin \theta \cos \varphi + y' \sin \theta \sin \varphi)} dx' dy', \quad (41)$$

$$\mathcal{J}_y^H(\theta, \varphi) = \iint_{S_A} H_{ay}(x', y') e^{j\beta(x' \sin \theta \cos \varphi + y' \sin \theta \sin \varphi)} dx' dy'. \quad (42)$$

From equations (37) and (38) it follows that the field components in the principal planes are

$$E_\theta(\theta, 0) = j\beta \frac{e^{-j\beta r}}{4\pi r} [\mathcal{J}_x^E(\theta, 0) + \mathcal{J}_y^H(\theta, 0) \cdot \eta \cos \theta] \quad (43)$$

$$E_\theta(\theta, 90^\circ) = j\beta \frac{e^{-j\beta r}}{4\pi r} [\mathcal{J}_y^E(\theta, 90^\circ) - \mathcal{J}_x^H(\theta, 90^\circ) \cdot \eta \cos \theta] \quad (44)$$

$$E_\phi(\theta, 0) = j\beta \frac{e^{-j\beta r}}{4\pi r} [-\eta \mathcal{J}_x^H(\theta, 0) + \mathcal{J}_y^E(\theta, 0) \cdot \cos \theta] \quad (45)$$

$$E_\phi(\theta, 90^\circ) = j\beta \frac{e^{-j\beta r}}{4\pi r} [-\eta \mathcal{J}_y^H(\theta, 90^\circ) - \mathcal{J}_x^E(\theta, 90^\circ) \cdot \cos \theta]. \quad (46)$$

The 3-D field dependence on the directional angles can be approximated from the 2-D dependences in the equations (43) through (46) as

$$\mathbf{E}(\theta, \varphi) \approx j\beta \frac{e^{-j\beta r}}{4\pi r} [\cos \varphi \cdot \mathbf{E}(\theta, 0) + \sin \varphi \cdot \mathbf{E}(\theta, 90^\circ)], \quad (47)$$

The total 3-D amplitude pattern of the field defined in (47) is obtained as

$$|\mathbf{E}(\theta, \varphi)| \approx \left\{ \cos^2 \varphi \cdot [E_\theta^2(\theta, 0) + E_\phi^2(\theta, 0)] + \sin^2 \varphi \cdot [E_\theta^2(\theta, 90^\circ) + E_\phi^2(\theta, 90^\circ)] + \sin(2\varphi) \cdot [E_\theta(\theta, 0) \cdot E_\theta(\theta, 90^\circ) + E_\phi(\theta, 0) \cdot E_\phi(\theta, 90^\circ)] \right\}^{1/2}. \quad (48)$$

In the pattern calculation, we drop the factor $j\beta e^{-j\beta r} / (4\pi r)$. Also, it can be shown that the last term in (48) is

$$E_\theta(\theta, 0)E_\theta(\theta, 90^\circ) + E_\phi(\theta, 0)E_\phi(\theta, 90^\circ) = (1 - \cos^2 \theta) \cdot [\mathcal{J}_x^E(\theta, 0)\mathcal{J}_y^E(\theta, 90^\circ) + \eta^2 \mathcal{J}_x^H(\theta, 90^\circ)\mathcal{J}_y^H(\theta, 0)]. \quad (49)$$

For high-directivity antennas, the angles θ , at which the antenna has significant pattern values, are small, and the term given in (49) can be neglected. Thus, the approximation of the 3-D pattern in terms of two orthogonal 2-D patterns reduces to the simple expression

$$|\mathbf{E}(\theta, \varphi)| \approx \sqrt{\cos^2 \varphi \cdot |\mathbf{E}(\theta, 0)|^2 + \sin^2 \varphi \cdot |\mathbf{E}(\theta, 90^\circ)|^2}. \quad (50)$$

Sometimes, the **phase pattern** of the far field is also measured. This requires phase reference and can be performed using vector network analyzers.

6. Gain Measurements*

The gain measurements require essentially the same environment as the pattern measurements. To measure the gain of antennas operating above 1 GHz, usually, anechoic chambers are used. Between 0.1 GHz and 1 GHz, ground-reflection ranges are used.

Below 0.1 GHz, directive antennas are very large and the ground effects become increasingly pronounced. Usually the gain at these frequencies is measured directly in the environment of operation. Same holds for high-frequency antennas operating in a complicated environment (mounted on vehicles or aircrafts).

We consider three gain-measurement techniques. The first two belong to the so-called *absolute-gain measurements*, and they are: the ***two-antenna method***, and the ***three-antenna method***. The third method is called the ***gain-transfer*** (or ***gain-comparison***) ***method***.

A. The two-antenna method

The ***two-antenna method*** is based on Friis transmission equation and it needs two identical samples of the tested antenna. One is the radiating antenna, and the other one is receiving. Assuming that the antennas are well matched in terms of impedance and polarization, the Friis transmission equation is

$$\frac{P_r}{P_t} = \left(\frac{\lambda}{4\pi R} \right)^2 G_t G_r, \text{ where } G_t = G_r = G, \quad (51)$$

or, in dB,

$$G_{\text{dB}} = \frac{1}{2} \left[20 \log_{10} \left(\frac{4\pi R}{\lambda} \right) + 10 \log_{10} \left(\frac{P_r}{P_t} \right) \right]. \quad (52)$$

One needs to know accurately the distance between the two antennas R , the received power P_r , the transmitted power P_t , and the frequency $f = c / \lambda$.

B. The three-antenna method

The ***three-antenna method*** is used when only one sample of the test antenna is available. Then, any other two antennas can be used to perform three measurements, which allow the calculation of the gains of all three antennas. All three measurements are made at a fixed known distance R between the

radiating and the transmitting antennas.

It does not matter whether an antenna is in a transmitting or in a receiving mode. What matters is that the three measurements involve all three possible pairs of antennas: antenna #1 and antenna #2; antenna #1 and antenna #3; antenna #2 and antenna #3. The calculations are again based on Friis transmission equation, which in the case of two different antennas (antenna $#i$ and antenna $#j$) measured during experiment $#k$ ($k = 1, 2, 3$) becomes

$$G_{i \text{ dB}} + G_{j \text{ dB}} = 20\log_{10}\left(\frac{4\pi R}{\lambda}\right) + 10\log_{10}\left(\frac{P_r}{P_t}\right)^{(k)}. \quad (53)$$

The system of equations describing all three experiments is

$$\begin{aligned} G_{1 \text{ dB}} + G_{2 \text{ dB}} &= 20\log_{10}\left(\frac{4\pi R}{\lambda}\right) + 10\log_{10}\left(\frac{P_r}{P_t}\right)^{(1)}, \\ G_{1 \text{ dB}} + G_{3 \text{ dB}} &= 20\log_{10}\left(\frac{4\pi R}{\lambda}\right) + 10\log_{10}\left(\frac{P_r}{P_t}\right)^{(2)}, \\ G_{2 \text{ dB}} + G_{3 \text{ dB}} &= 20\log_{10}\left(\frac{4\pi R}{\lambda}\right) + 10\log_{10}\left(\frac{P_r}{P_t}\right)^{(3)}. \end{aligned} \quad (54)$$

The right-hand sides of the equations in (54) are known if the distance R and the ratios of the received-to-transmitted power are known. Thus, the following system of three equations with three unknowns is obtained

$$\begin{cases} G_{1 \text{ dB}} + G_{2 \text{ dB}} = A \\ G_{1 \text{ dB}} + G_{3 \text{ dB}} = B \\ G_{2 \text{ dB}} + G_{3 \text{ dB}} = C \end{cases} \quad (55)$$

The solution to the system of equations in (55) is

$$\begin{aligned} G_{1 \text{ dB}} &= \frac{A + B - C}{2}, \\ G_{2 \text{ dB}} &= \frac{A - B + C}{2}, \\ G_{3 \text{ dB}} &= \frac{-A + B + C}{2}. \end{aligned} \quad (56)$$

C. The gain-comparison method

The **gain-comparison method** requires an antenna the gain of which is exactly known (called **gain standard**) and a transmitting antenna the gain of which does not need to be known. Two sets of measurements are performed.

- 1) The test antenna is in a receiving mode, and its received power P_{AUT} is measured.
- 2) The gain standard is in a receiving mode in exactly the same arrangement (the distance R and the transmitted power P_0 are kept the same), and its received power P_{GS} is measured.

In both measurements, the receiving antennas must be matched to their loads (the receiver).

The calculation of the test antenna gain in dB uses Friis' transmission equation. The two measurements lead to the following system of equations:

$$\begin{aligned} G_{AUT \text{ dB}} + G_0 \text{ dB} &= 20\log_{10}\left(\frac{4\pi R}{\lambda}\right) + 10\log_{10}\left(\frac{P_{AUT}}{P_0}\right)^{(1)}, \\ G_{GS \text{ dB}} + G_0 \text{ dB} &= 20\log_{10}\left(\frac{4\pi R}{\lambda}\right) + 10\log_{10}\left(\frac{P_{GS}}{P_0}\right)^{(2)}. \end{aligned} \quad (57)$$

Here,

$G_{AUT \text{ dB}}$ is the gain of the test antenna;

$G_{GS \text{ dB}}$ is the gain of the gain standard; and

$G_0 \text{ dB}$ is the gain of the transmitting antenna.

From (57), we derive the expression for the gain of the test antenna:

$$G_{AUT \text{ dB}} = G_{GS \text{ dB}} + 10 \cdot \log_{10}\left(\frac{P_{AUT}}{P_{GS}}\right). \quad (58)$$

If the test antenna is circularly or elliptically polarized, two orthogonal linearly polarized gain standards must be used in order to obtain the partial gains corresponding to each linearly polarized component. The total gain of the test antenna is

$$G_{AUT \text{ dB}} = 10\log_{10}(G_{AUTv} + G_{AUTh}), \quad (59)$$

where G_{AUT_v} is the dimensionless gain of the test antenna measured with the vertically polarized gain standard and G_{AUT_h} is the dimensionless gain of the test antenna measured with the horizontally polarized gain standard.

7. Directivity Measurements*

The directivity measurements are directly related to the pattern measurements. Once the pattern is found over a sphere, the directivity can be determined using the definition:

$$D_0 = 4\pi \frac{F_{\max}(\theta_0, \varphi_0)}{\int_0^{2\pi} \int_0^\pi F(\theta, \varphi) \sin \theta d\theta d\varphi}, \quad (60)$$

where $F(\theta, \varphi)$ is the power pattern of the test antenna and (θ_0, φ_0) is the direction of maximum radiation.

Generally, $F(\theta, \varphi)$ is measured by sampling the field over a sphere of constant radius R . The spacing between the sampling points depends on the directive properties of the antenna and on the desired accuracy. The integral

$$\Pi = \int_0^{2\pi} \int_0^\pi F(\theta, \varphi) \sin \theta d\theta d\varphi \quad (61)$$

is computed numerically, e.g.,

$$\Pi \approx \frac{\pi}{N} \frac{2\pi}{M} \sum_{j=1}^M \left[\sum_{i=1}^N F(\theta_i, \varphi_j) \sin \theta_i \right]. \quad (62)$$

If the antenna is circularly or elliptically polarized, two measurements of the above type must be carried out in order to determine the partial directivities, D_θ and D_φ . Then, the total directivity is calculated as

$$D_0 = D_\theta + D_\varphi, \quad (63)$$

where the partial directivities are defined as

$$D_\theta = 4\pi \frac{F_{\theta \max}}{\Pi_\theta + \Pi_\varphi}, \quad (64)$$

$$D_\phi = 4\pi \frac{F_{\phi\max}}{\Pi_\theta + \Pi_\phi}. \quad (65)$$

8. Radiation Efficiency, e_{cd} *

In order to calculate the radiation efficiency, the gain and the directivity must be measured first. Factors like impedance mismatch and polarization mismatch have to be minimized during these measurements. The radiation efficiency is then calculated using its definition:

$$e_{cd} = \frac{\text{Gain}}{\text{Directivity}}. \quad (66)$$

9. Impedance Measurements*

The input impedance of an antenna is calculated via the reflection coefficient at its terminals Γ , which are connected to a transmission line of known characteristic impedance Z_c . If the magnitude and the phase of Γ are known, then, the antenna input impedance is calculated as

$$Z_A = Z_c \left(\frac{1+\Gamma}{1-\Gamma} \right), \Omega. \quad (67)$$

Γ is usually measured using a vector network analyzer (VNA). The VNA measures the complex S -parameters of microwave networks. The antenna is a single-port device, therefore, $\Gamma = S_{11}$.

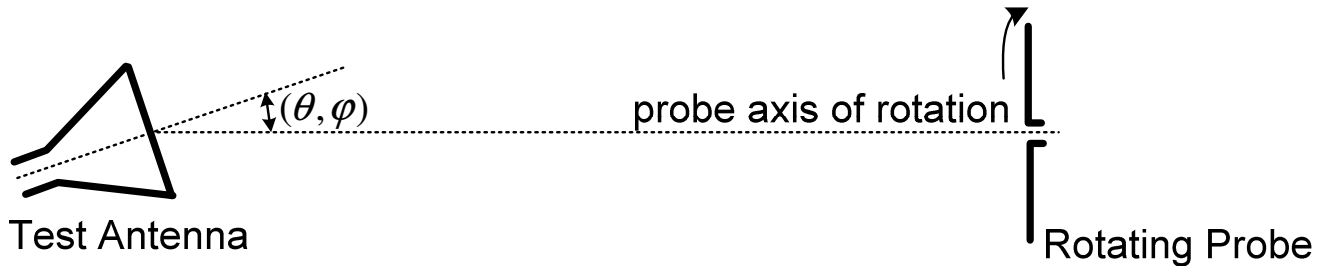
10. Polarization Measurements*

A complete description of the antenna polarization is given by the polarization ellipse (the axial ratio and the tilt angle), as well as the sense of rotation (clockwise, or counter-clockwise). In general, the polarization of an antenna is not the same in every direction, i.e., it depends on the observation angle. That is why, often, many measurements are required according to the desired degree of polarization description.

The polarization measurement methods are classified into three general categories.

- **Partial methods** give incomplete information about the polarization but are simple and require conventional equipment.
- **Comparison methods** yield complete polarization information; however, they require a polarization standard.
- **Absolute methods** yield complete polarization information; and, they do not require a polarization standard.

The **polarization-pattern method** is a common partial method. It produces the polarization ellipse parameters (the axial ratio and the tilt angle) in a given direction of radiation. It cannot determine however the sense of rotation. The AUT can be either in transmitting or in receiving mode. The other antenna (the probe) must be linearly polarized, e.g., a dipole, and its pattern must be accurately known. A typical arrangement for the polarization-pattern measurement is given below.

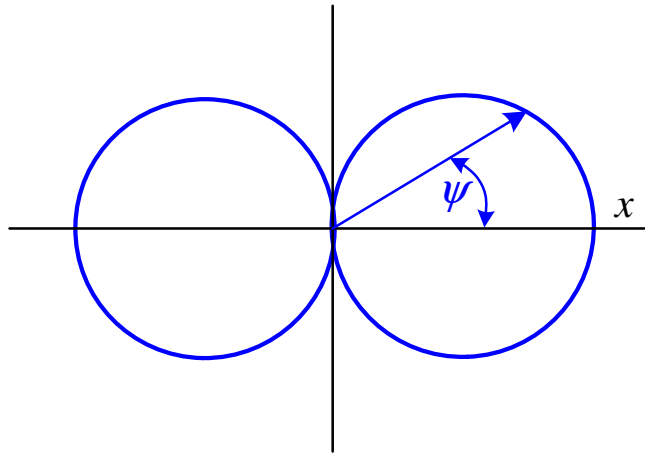


The signal at the output of the probe depends on the PLF for the test and probe antennas. This PLF is determined by two factors: the polarization vector of the test antenna $\hat{\rho}_{AUT}$ and the angle of the probe's rotation ψ , which is also the angle of the probe's polarization vector $\hat{\rho}_{PA}$ relative to a chosen reference angle. Since the probe has linear polarization, we can state that

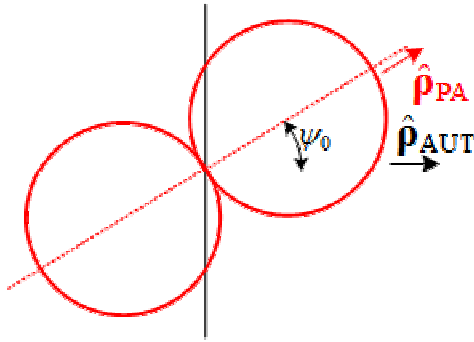
$$\hat{\rho}_{PA}(\psi) = \hat{x} \cos \psi + \hat{y} \sin \psi. \quad (68)$$

The axes x and y must be perpendicular to the line connecting the two antennas. The signal level is recorded and plotted versus the angle of rotation ψ . This is the **polarization pattern** in the considered direction of radiation.

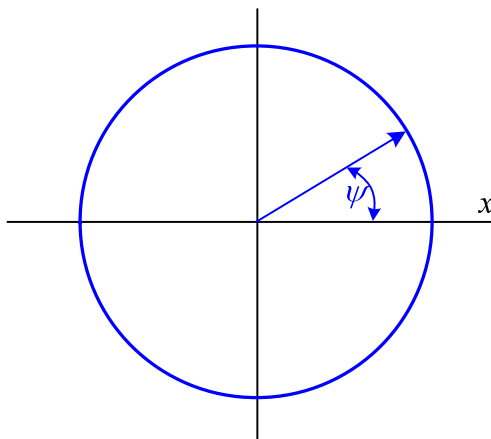
Let us first consider the case of an AUT which is linearly polarized with a polarization vector $\hat{\rho}_{AUT} = \hat{x}$. Then the PLF is $|\hat{\rho}_{PA} \cdot \hat{\rho}_{AUT}^*|^2 = \cos^2 \psi$. The figure below shows the polar plot of this PLF. This PLF pattern is the AUT polarization pattern.



In general, if the AUT is linearly polarized, the polarization pattern will be the same as the cosine pattern shown above but it may be tilted depending on the initial angle ψ_0 between the polarization axes of the probe and the AUT; see the illustration below.



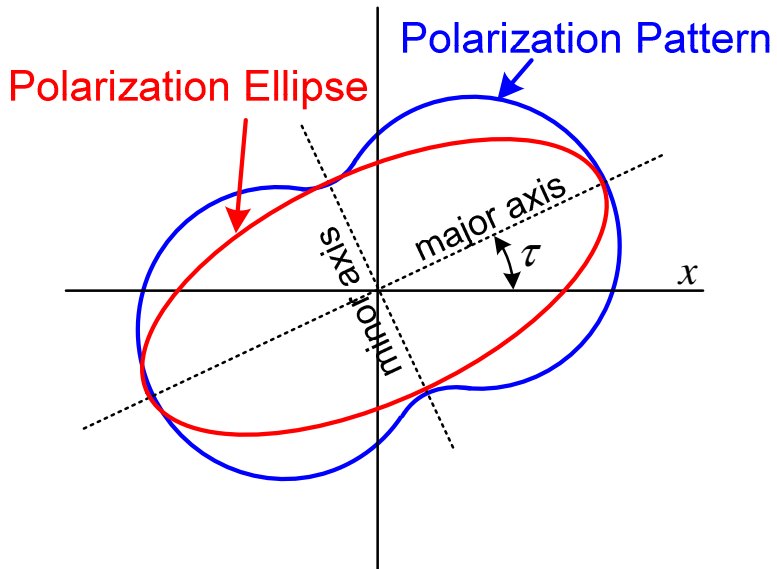
If the AUT is circularly polarized, the polarization pattern is a circle regardless of the initial mutual orientation of the probe and the AUT (see the illustration below).



This follows from the PLF derivation as:

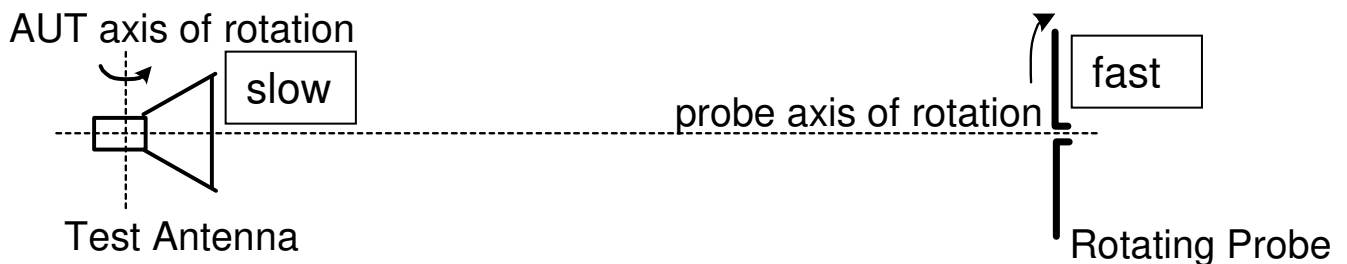
$$PLF(\psi) = |(\hat{\mathbf{x}} \cos \psi + \hat{\mathbf{y}} \sin \psi) \cdot (\hat{\mathbf{x}} \pm j\hat{\mathbf{y}}) / \sqrt{2}|^2 = |\cos \psi \pm j \sin \psi|^2 / 2 = 0.5. \quad (69)$$

In the general case of an elliptically polarized AUT, the polarization pattern is a dumb-bell contour, which allows for the direct calculation of the axial ratio and the tilt angle τ of the polarization ellipse as is shown in the figure below.



The polarization-pattern method cannot provide information about the sense of rotation. However, this can be easily established by the use of circularly polarized probes (e.g. spiral antennas): one of a clockwise polarization, and the other one of a counter-clockwise polarization. Whichever receives a stronger signal determines the sense of rotation.

Another partial method is the ***axial-ratio pattern method***. The arrangement is very similar to that of the polarization-pattern method. The only difference is that now the AUT (which is usually in a receiving mode) is rotated in θ or ϕ by the antenna positioner. The probe rotates in the polarization plane (this plane is perpendicular to the line connecting the two antennas) with much larger angular speed than the AUT so as to complete one full turn at approximately every degree of rotation of the test antenna.



As a result of the measurement described above, a 2-D pattern is obtained in θ or ϕ , which allows for the calculation of the axial ratio of the polarization at any observation direction. Such a pattern (in dB) of an antenna, which is nearly circularly polarized along $\theta = 0$, is shown below.

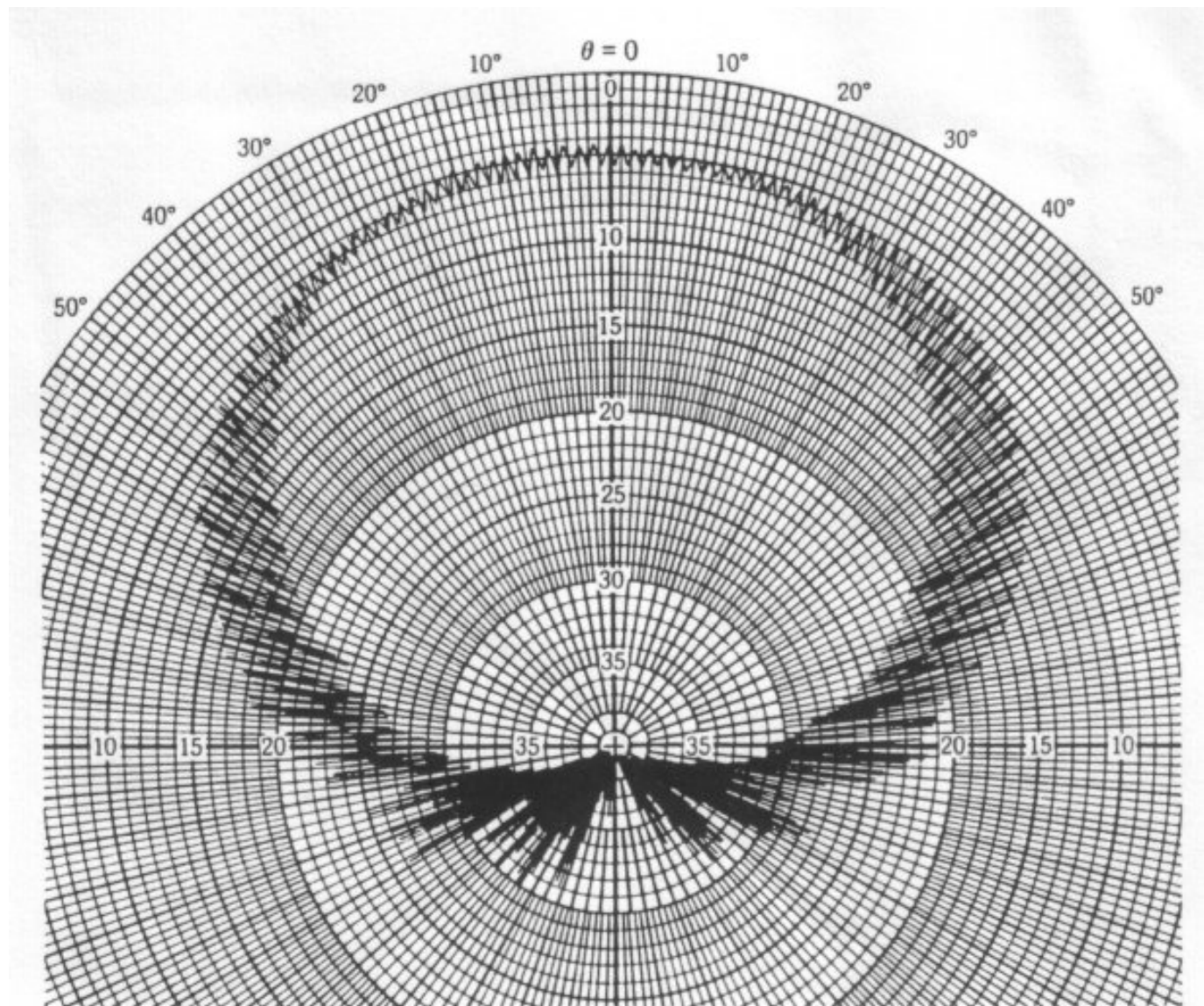


Figure 16.26 Pattern of a circularly polarized test antenna taken with a rotating, linearly polarized, source antenna [E. S. Gillespie, "Measurement of Antenna Radiation Characteristics on Far-Field Ranges," in *Antenna Handbook* (Y. T. Lo & S. W. Lee, eds.), 1988, © Van Nostrand Reinhold Co., Inc.]

[Balanis]

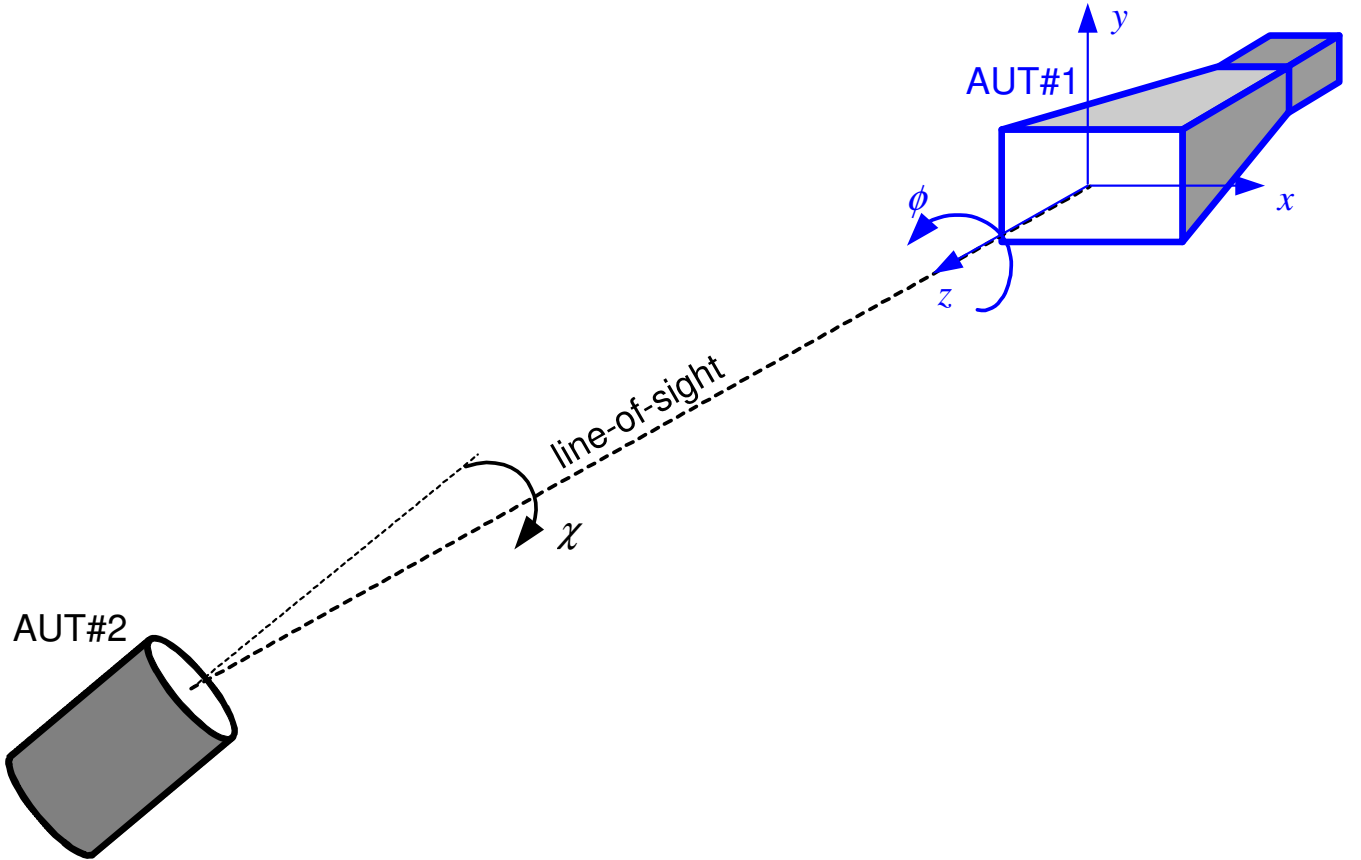
From the plot above, it is obvious that the axial-ratio pattern has an inner envelope and an outer envelope. The ratio of the outer envelope to the inner one for a given angle gives the axial ratio of the field polarization in this direction. For example, the pattern above shows that the test antenna is nearly circularly polarized along boresight ($\theta = 0$), where the axial ratio is close to one. At greater observation angles, however, its polarization becomes elliptical of increasingly larger axial ratio.

The axial-ratio pattern method yields only the axial ratio of the polarization ellipse. It does not give information about the tilt angle and the sense of rotation. However, it is very fast and convenient to implement in any antenna test range. The tilt angle at selected directional angles can be always clarified later with the polarization-pattern method. The sense of rotation can also be determined in a subsequent measurement with circularly polarized probes.

The most general absolute polarization measurement method is the ***three-antenna method***. It yields full polarization information for all three antennas. The only *a-priori* knowledge required is the approximate tilt angle of one of the three antennas.

The method requires the measurement of the amplitude and the phase of the normalized received voltage in three experiments, which involve: 1) antenna #1 and antenna #2; 2) antenna #1 and antenna #3; and 3) antenna #2 and antenna #3. All three experiments must use the same measurement set-up. The three complex voltage phasors are measured as a function of the angles ϕ and χ , which are the angles of rotation of the antennas about the antenna-range axis (the line connecting the antenna centers).

An example set-up is shown in the figure below. First, the AUT#1 is scanned for $\phi \in [0^\circ, 360^\circ]$ usually with a step of $\Delta\phi = 1^\circ$. Then, the angle of AUT#2 is incremented by $\Delta\chi$ (usually, $\Delta\chi \approx 15^\circ$) and AUT#1 is scanned again for $\phi \in [0^\circ, 360^\circ]$. This is repeated until the angle χ sweeps the whole range from 0° to 360° .



Three complex quantities $M_{m,n}$ are then calculated from the double Fourier transform of the voltage phasor patterns:

$$M_{m,n} = \frac{\int_0^{2\pi} \int_0^{2\pi} \tilde{V}_{m,n}(\phi, \chi) e^{+j(\phi+\chi)} d\phi d\chi}{\int_0^{2\pi} \int_0^{2\pi} \tilde{V}_{m,n}(\phi, \chi) e^{-j(\phi+\chi)} d\phi d\chi}, \quad (m, n) = (1, 2), \text{ or } (1, 3), \text{ or } (2, 3). \quad (70)$$

It can be shown (see references [6],[7],[8]) that $M_{m,n}$ are equal to the dot products of the circular polarization ratios (see reference [3]; for definition of polarization ratio refer to Lecture 5, eq. 5.21) of the two antennas used in the respective measurement:

$$\begin{aligned} \hat{\rho}_{c1} \cdot \hat{\rho}_{c2} &= M_{1,2} \\ \hat{\rho}_{c1} \cdot \hat{\rho}_{c3} &= M_{1,3} \\ \hat{\rho}_{c2} \cdot \hat{\rho}_{c3} &= M_{2,3} \end{aligned} \quad (71)$$

The system in (71) is used to solve for the three circular polarization ratios:

$$\hat{\mathbf{p}}_{c1} = \sqrt{\frac{M_{12}M_{13}}{M_{23}}}; \quad \hat{\mathbf{p}}_{c2} = \sqrt{\frac{M_{12}M_{23}}{M_{13}}}; \quad \hat{\mathbf{p}}_{c3} = \sqrt{\frac{M_{23}M_{13}}{M_{12}}} \quad (72)$$

The square root of a complex number implies ambiguity in the phase calculations for the polarization vectors. This is why we need to have an approximate knowledge of the tilt angle of one of the antennas. The circular polarization ratios are directly related to the polarization ellipse; see Lecture 5, [2], [3].

References

- [1] *IEEE Standard Test Procedures for Antennas*, IEEE Std 149-1979, IEEE Inc., 1979, distributed by Wiley-Interscience.
- [2] J.S. Hollis, T.J. Lyon, and L. Clayton, Jr., *Microwave Antenna Measurements*, Scientific-Atlanta, Inc., Atlanta, Georgia, July 1970.
- [3] W.H. Kummer and E.S. Gillespie, “Antenna measurements-1978,” *Proc. IEEE*, vol. 66, No. 4, pp. 483-507, April 1978.
- [4] C.A. Balanis, *Antenna Theory*, 2nd ed., John Wiley & Sons, Inc., New York, 1997.
- [5] J. Kraus, *Antennas*, 2nd ed., McGraw Hill, Inc., New York, 1988.
- [6] J.R. Jones and D.W. Hess, “Automated three-antenna polarization measurements using digital signal processing,” white paper available for download at <http://www.mi-technologies.com/techliterature/>
- [7] E.B. Joy, and D.T. Paris, “A practical method for measuring the complex polarization ratio of arbitrary antennas,” *IEEE Trans. on Antennas and Propagation*, vol. AP-21, pp. 432-435, 1973.
- [8] A.C. Newell, and D.M. Kerns, “Determination of both polarization and power gain of antennas by a generalised 3-antenna measurement method,” *Electronics Letters*, vol. 7, No. 3, pp. 68-70, February 11, 1971.